

The Redshift Evolution of the Metagalactic Ionizing Flux Inferred from Metal Line Ratios in the Lyman Forest

Antoinette Songaila¹

Institute for Astronomy, University of Hawaii, 2680 Woodlawn Drive, Honolulu, HI 96822

To be published in *Astronomical Journal*, 6/98

ABSTRACT

Metal line ratios in a sample of 13 quasar spectra obtained with the HIRES spectrograph on the KeckI telescope have been analyzed to characterize the evolution of the metagalactic ionizing flux near a redshift of 3. The evolution of Si IV/C IV has been determined using three different techniques: using total column densities of absorption line complexes, as in Songaila & Cowie (1996); using the column densities of individual Voigt profile components within complexes; and using direct optical depth ratios. All three methods show that Si IV/C IV changes abruptly at $z \sim 3$, requiring a jump in value of about a factor of 3.4, and indicating a significant change in the ionizing spectrum that occurs rapidly between $z = 2.9$ and $z = 3$, just above the redshift at which Reimers et al. (1997) detected patchy He II Ly α absorption. At lower redshifts, the ionization balance is consistent with a pure power law ionizing spectrum but at higher redshifts the spectrum must be very soft, with a large break at the He⁺ edge. An optical depth ratio technique is used to measure the abundances of ions whose transitions lie within the forest and C III, Si III and O VI are detected in this way. The presence of a significant amount of O VI at $z > 3$ suggests either a considerable volume of He III bubbles embedded in the more general region where the ionizing flux is heavily broken, or the addition of collisional ionization to the simple photoionization models.

Subject headings: early universe — intergalactic medium — quasars: absorption lines — galaxies: formation

¹The author was a visiting astronomer at the W. M. Keck Observatory, jointly operated by the California Institute of Technology and the University of California.

1. Introduction

Whereas we know from the absence of any significant Gunn-Peterson effect even in the highest redshift quasars that hydrogen reionization of the intergalactic gas must have taken place at $z > 5$, we have much less information about the period at which the bulk of singly ionized helium converted to doubly ionized helium. Since late He^+ ionization may significantly change the temperature of the intergalactic gas it is critical to understand this heating if we are to correctly model the growth of structure in the IGM, and determine the mapping of the baryon density to observable quantities such as observations of the neutral hydrogen $\text{Ly}\alpha$ forest and the He^+ $\text{Ly}\alpha$ opacity. Phenomenological modelling of this event depends critically on the softness of the composite spectrum of the ionizing sources (e.g. Miralda-Escudé & Rees 1993; Madau & Meiksin 1994), amplified by the subsequent radiative transfer, and such models cannot be considered reliable in predicting the high energy ($E > 54$ eV) metagalactic ionizing spectrum above the He^+ ionization edge, which determines the fraction of singly ionized helium.

Our most direct information on the He^+ opacity is through observations of quasars whose spectra extend to the He^+ $\text{Ly}\alpha$ wavelength. Despite the extreme difficulty of these measurements, successful observations of the He^+ $\text{Ly}\alpha$ absorption have been made toward $z > 2.8$ quasars with HST (Jakobsen et al. 1994; Hogan et al. 1997; Reimers et al. 1997) and of the $z = 2.72$ quasar HS1700+6416 with HUT (Davidsen et al. 1996; Zheng et al. 1998). The He^+ $\text{Ly}\alpha$ opacity shows a marked decrease from a value of $\tau = 3.2_{-1.1}^{+\infty}$ in Q0302–003 at $z = 3.29$ to $\tau = 1.0 \pm 0.07$ in HS1700+6416. More remarkably, the Reimers et al. observation of the intermediate redshift quasar HE2347–4342 at $z = 2.89$ shows both ‘troughs’ and ‘voids’ in the He II $\text{Ly}\alpha$ observations, suggesting that at $z \sim 2.8$ we are seeing fully ionized He III bubbles interspersed among as yet unionized He^+ regions and that it is at this point that the porosity of He III regions is approaching unity.

The recent discovery that the bulk of $\text{Ly}\alpha$ forest absorption with $N(\text{H I}) > 3 \times 10^{14} \text{ cm}^{-2}$ contains associated metals (Songaila & Cowie 1996, hereafter SC) gives us an alternative approach to the problem since ionization balance in these forest metals provides a diagnostic of the shape of the metagalactic flux in the neighborhood of the He^+ edge. As was first noted in Songaila et al. (1995), the value of Si IV/C IV in high ionization systems is critically dependent on the He^+ ionization edge break strength. This has subsequently been investigated in more detail by SC, Savaglio et al. (1997) and Giroux & Shull (1997), among others. As will be discussed further here, the bulk of the forest metal line systems at the currently observed redshifts ($z \sim 2 - 4$) are high ionization (C II/C IV $\ll 0.1$) and so, unless there is a strong break at the edge, they will have Si IV/C IV $\ll 0.1$ even for the higher Si/C abundances characteristic of low metallicity systems. Therefore, once the He^+ is fully ionized

and the IGM becomes relatively transparent to the integrated quasar spectrum (e.g. in the metagalactic spectrum of Haardt & Madau 1996), the observed Si IV/C IV values should fall in this low range. SC and Savaglio et al. (1997) have shown that, whereas this is generally true at $z < 3$, much higher Si IV/C IV values are regularly seen at $z > 3$, suggesting a significant change above this redshift, which would be consistent with the interpretation of the Reimers et al. (1997) observations as showing the redshift at which He III bubbles begin to overlap. Boksenberg (1998) has recently questioned this result, based on an analysis of the the redshift evolution of the ion ratios in the separate Voigt profile components in complex systems rather than in the integrated column densities of the complexes. However, his analysis is based on rather a small sample of systems without clear selection criteria. In this paper, I shall use the largest sample to date to demonstrate unambiguously that, irrespective of the method of analysis, there is indeed a rapid jump in the value of SI IV/C IV at a redshift just below 3, and that the ionization stages in the metals are consistent with this being, for most systems, the point at which they change from being ionized by a metalgalactic spectrum that is, at $z > 3$, heavily broken above 54 eV to one that is only mildly broken at the lower redshifts.

The sample and the data reduction are described in §2 and the reader who is primarily interested in the results could safely skip this section. The evolution of the C II/C IV and Si IV/C IV values with redshift is described in §3 where I show that the presence of a jump in Si IV/C IV values at z just under 3 is highly significant and does not depend on the method of analysis, whether by total column densities of complex, by the column densities of individual Voigt components, or by directly analyzing the distribution of optical depth ratios. In §4 I consider the overall ionization balance including intermediate ionization stages such as C III and Si III and high ions such as N V and O VI using, for those lines that lie primarily within the forest, the optical depth distributions of the ensembles of such lines, which provides a new and robust technique for determining their properties. The overall ionization balance is broadly consistent with unbroken power law photoionization at $z < 3$; however, the observation of significant amounts of O VI at $z > 3$ requires either the presence of a considerable volume of He III bubbles permeating regions where the ionizing flux is heavily broken, or the addition of collisional ionization to the simple photoionization models. Finally, the conclusions are briefly summarised in §5.

2. Data

The sample was drawn from observations of 13 quasars with complete or near-complete coverage between the quasars' Lyman alpha and C IV emission lines. All observations (sum-

marised in Table 1) were made with the HIRES spectrograph on the KeckI 10m telescope, using a $1.14'' \times 7''$ slit, which gives a resolution of $R = 37,000$, and with total exposure times from 3.3 hours to just over 10 hours. The approximate S/N per resolution element for each quasar at wavelengths between Ly α and C IV emission is summarised in Table 1 and ranges from 60 (Q0256–000) to 330 (Q1422+231).

Individual exposures were generally set to 40 minutes (providing a reasonable compromise between minimizing cosmic ray hits and read noise effects) and with the 2048 Tektronix CCD read out with a binning of two in the spatial direction and one in the spectral direction, resulting in a spatial pixel of $0.38''$ and $\Delta\lambda/\lambda = 7.3 \times 10^{-6}$; this substantially oversamples the resolution element. For the higher redshift quasars several settings of the HIRES cross-disperser were used to provide the full wavelength coverage. All but three of the quasars have full coverage of the wavelength region of interest (Table 1, column 4) and the remaining three have small interorder gaps. In general, the spectra extend from approximately 3800 \AA , below which the HIRES sensitivity begins to fall rapidly, up to the wavelength of the quasar’s C IV emission. A white dwarf star and the thorium-argon calibration lamp were also observed either immediately before or immediately after each sequence of exposures on a quasar.

A relatively straightforward extraction technique was used since optimization does not provide substantial gains for these spatially undersampled and signal-dominated spectra. Starting from approximate order and wavelength solutions, the position and shape of each order on the CCD was determined from the observations of the white dwarf. Only orders lying fully on the CCD were extracted. A small number of known bad points and columns were cleaned by interpolation, and a number of regions, such as the central blemish on the chip, flagged as unusable. The first pass cosmic ray rejection was made by forming a residual image with a 5-point two-dimensional median subtracted and then subtracting an 11-point row by row median. Any points in this differenced image that exceeded expected values by more than 4σ were interpolated from neighboring points along the column (spatial) direction.

The spectral image was distorted by bilinear interpolation to make the echelle order parallel to the rows. The sky was then determined from the median of pixels on the same column lying between $2''$ and $3.5''$ on either side of the maximum signal, and subtracted from the spectral image, and the spectrum was extracted in a $\pm 1''$ window. The spectra for all the sub-exposures were then combined with an optimal S/N weighting, and any residual cosmic ray structure was removed by identifying any strongly deviant ($> 5 \sigma$) points in the individual spectrum and flagging and removing these from a second and final summation. The blaze function was determined from a normalised fifth-order polynomial fit to the white

dwarf spectrum, iteratively repeated to exclude any absorption lines, and divided into the spectrum. The wavelength and spectrum for each order were then individually stored.

The Th-Ar calibration spectrum was extracted in the same fashion as the object spectrum but without any sky subtraction step. For each order, each of the stronger unblended calibration lines was fitted with a gaussian to determine its centroid, and a third-order polynomial fit was then applied to determine the wavelength solution. From 10 to 30 calibration lines were used for each order and the r.m.s. residual was normally less than 2×10^{-3} Å, so that velocities should be accurate to better than 0.1 km s^{-1} . Finally, the wavelength scale was converted to vacuum heliocentric, which is used throughout the present paper.

A typical extracted order longward of the forest is shown in Figure 1a which shows order 63 from a 2-hr exposure of Q1159+123, obtained as three 40-minute exposures in 1997 April. The absorption lines in the center of the order are a C IV doublet, and the rise in flux to shorter wavelengths reflects the onset of the quasar’s Ly α and N V emission. Figure 1b shows an order in the forest blueward of the quasar’s Ly α emission, where the accuracy of the sky subtraction may be gauged from the precision with which the bases of the saturated lines approach zero.

A final combined spectrum was made from all the observations taken at all echelle settings, with spectra covering each order added in a S/N optimized fashion to form a combined spectrum of that order. The final 8-hr spectrum of order 63 in Q1159+123 is shown in Figure 2 for comparison with Figure 1a. An associated effective exposure time vector, normalised by the S/N, was also maintained at each point; this can be combined with the counts to determine the noise at each point in the spectrum. For some purposes it is useful to have a combined spectrum and this was formed by interpolating all the orders to a uniform (0.05 Å) grid which provides Nyquist sampling throughout the wavelength range. A typical spectrum (of Q1159+123) is shown as Figure 3. This spectrum has a Lyman limit system just longward of 4150 Å and stretches through to C IV emission just below 7000 Å, near the atmospheric A band, which can be clearly seen in the spectrum. Most of the remaining features between Ly α and C IV emission are C IV absorption line doublets.

For most purposes normalized (continuum fitted) spectra from each order were used. The continuum fitting is made on a $\pm 2000 \text{ km s}^{-1}$ region of interest by iterating a second-order polynomial fit to a 10-point smoothed spectrum and rejecting significantly deviant regions ($|\Delta(\text{spectrum})/\text{fit}| > 0.025$). The fit to the region around a C IV complex at $z = 3.26101$ in Q1159+123 is shown in Figure 4. Multiple Voigt profiles were then fitted to the absorption line profiles using the IDL version of Bevington’s CURVEFIT algorithm.

3. Line Ratio Evolution with Redshift

3.1. Introduction

Each quasar spectrum was first searched for all complexes of C IV doublets redward of the $\text{Ly}\alpha$ forest and outside of the quasar’s proximity zone, defined to stretch to -4000 km s^{-1} blueward of the quasar’s redshift. The sample was then restricted to those cases for which Si IV also lies redward of the quasar’s $\text{Ly}\alpha$ emission. The redshift range used for each quasar is summarised in Table 1. Voigt profiles were next fitted to each such complex. The choice of the number of Voigt components is somewhat arbitrary because of the problems of blending but the complexes are quite weak in general and in the absence of saturation the integrated column densities of complexes should be well determined. In the same way, integrated column densities or upper limits for Si IV, C II and Si II were determined for lines lying longward of the forest. The usable redshift range for C II is also shown in Table 1. The profile fits to the C IV and Si IV doublets in all the cloud complexes with $10^{13} \text{ cm}^{-2} < N(\text{C IV}) < 10^{14} \text{ cm}^{-2}$ are shown in Figure 5. The redshifts, number of Voigt components (a minimum of two was used), C IV column density, Si IV column density, and C II and Si II column densities (where these lines are redward of the forest) are summarised for all complexes with $N(\text{C IV}) > 5 \times 10^{12} \text{ cm}^{-2}$ in Table 2.

3.2. Evolution of total column density ratios

Figure 6 shows the evolution of the integrated value of Si IV/C IV in the 76 complexes with $5 \times 10^{12} \text{ cm}^{-2} \leq N(\text{C IV}) \leq 10^{14} \text{ cm}^{-2}$ as well as in the the higher redshift systems satisfying this condition in Savaglio et al.’s (1996) observations of Q0000–263. As SC and Savaglio et al. (1996) previously noted, Si IV/C IV increases considerably between $z = 2$ and $z = 4$, with a strong suggestion of a break in the distribution of values around $z = 3$. In contrast, the C II/C IV ratio shown in Figure 7 does not exhibit this behaviour: in most of the complexes where C II/C IV can be measured, it is weak (C II/C IV < 0.1) or undetected, regardless of redshift. Median values of Si IV/C IV are shown as a function of redshift in Figure 8. The median ratio is $0.039_{-0.006}^{+0.009}$ for all the systems below $z = 3$ but $0.13_{-0.04}^{+0.04}$ above $z = 3$, where the errors are 1σ computed using the median sign method. A key diagnostic in interpreting the data is whether the evolution is in the form of a step function or is a smoother change with redshift. A discontinuous change might arise from the effects of a change in the metagalactic ionizing spectrum at the He^+ ionization edge, whereas a smoother evolution might follow from the more general evolution of the external ionizing field and the range of internal densities and internal ionization in the complexes. The data

of Figure 6 and Figure 8 are strongly suggestive of an abrupt transition between $z = 2.9$ and $z = 3$. This redshift is slightly higher than, but comparable to, the redshift ($z = 2.8$ to 2.9) below which He II would be inferred to be predominantly ionized to He III from the direct observations of the He II Ly α forest (Reimers et al. 1997).

To quantify this, distribution functions of Si IV/C IV have been formed for complexes with $z = 2.75 - 2.95$, just below the suspected break, and for $z = 3.0 - 3.2$, just above it. The histograms of Si IV/C IV values for the 16 systems in the low redshift interval and the 22 systems in the high redshift interval are shown in Figure 9. The median value of $0.038^{+0.029}_{-0.010}$ at $2.75 < z < 2.95$ is consistent with that of all the $z < 3$ systems, whereas the $3.0 < z < 3.2$ median value of $0.14^{+0.04}_{-0.075}$ is consistent with that of all the $z > 3$ systems. Moreover, a rank sum test shows that the $z = 2.75 - 2.95$ data are consistent with being drawn from the same distribution as the $z < 2.75$ systems, and the $z = 3.0 - 3.2$ data with being drawn from the same distribution as the $z > 3.2$ systems. However, the rank sum test shows that the $z = 3.0 - 3.2$ data has a probability of only 2.2×10^{-4} of being drawn from the same distribution as the $z = 2.75 - 2.95$ data, and that at the 98% confidence level the data require a jump of at least a multiplicative factor of 1.8 from the lower to the higher redshift interval. The data are therefore consistent with invariant distributions at high and low redshift together with an abrupt jump between $z = 2.9$ and $z = 3$. The corresponding step function, with Si IV/C IV changing by a factor of 3.4 at $z = 2.95$, is shown as the dashed line in Figure 8.

Assuming instead that the evolution of the median ionization ratio is a smooth power law in $(1+z)$ requires an evolution of the form $(1+z)^{5.4}$ which is shown as the dotted line in Figure 8. This however predicts a jump of only 1.57 between $z = 2.85$ and $z = 3.1$ which, as already noted, is not large enough to reconcile the relative distribution functions of Figure 9. It would therefore seem that simple smooth power law evolution is not consistent with the data.

3.3. Internal structure

Variations of the ionization ratios in different regions within a complex can result from structure in the internal density of material in the complex, or from the presence of internal ionization sources. It is therefore of considerable interest to examine the ionization ratios within the complexes to understand how these effects can contribute to the overall ionization balance and to determine whether or not this can change the conclusions of section 3.2.

The simplest approach to this is to break down the complexes into the components

determined by Voigt profile fitting (Boksenberg 1998). Figure 10 shows the redshift evolution of the Si IV/C IV components broken down in this way. All components with $N(\text{C IV}) > 5 \times 10^{12} \text{ cm}^{-2}$ have been included irrespective of the total column density of the complex, so that a small number of high density complexes provide a large number of components, and these also include a number of Lyman limit systems in which radiative transfer effects are significant. However, even with these effects and with the increased confusion owing to the large spread in components, the change between high and low redshifts is clearly seen. Figure 11 shows histograms of the distributions above and below $z = 3$. If the components are considered to be statistically independent samples then the median ratio is $0.043_{-0.008}^{+0.015}$ below $z = 3$ and $0.15_{-0.04}^{+0.04}$ above $z = 3$. At the 98% confidence level, the minimum multiplicative increase to bring the distributions into consistency is 1.93.

However, the methodology of fitting Voigt profiles is a very unsatisfactory approach to this problem because of the considerable arbitrariness in the choice of components, which can have several unfortunate effects, including forcing other ions preferentially into or out of a particular component, blending components, and introducing non-independent components. These problems can be avoided by using the more direct technique of computing the ratios of the optical depths of various ions throughout the complex. This procedure is illustrated in Figures 12 and 13. For each identified C IV complex, all data points lying above some limiting optical depth (here $\tau(\text{C IV } 1550) > 0.05$) were identified, and optical depths in the corresponding regions of the other ions were then measured. Si IV and C IV optical depths for a complex at $z = 3.33714$ in 2000–330 are shown in Figure 12. The ratio $(\tau\lambda f)$ relative to that of C IV then gives the ratio of $N(\text{ion})/N(\text{C IV})$ throughout the velocity range of the complex, as is illustrated in Figure 13, where it is compared with the average ion ratios in the complex, shown as the solid line. This procedure can be slightly in error if there is a substantial amount of thermal broadening but should be adequate for these heavier elements where the broadening is primarily kinematic. Si IV/C IV values determined in this way for all the complexes of Table 2 is shown in Figure 14 where again a clear evolution of the distribution can be seen.

In order to determine the noise levels associated with this procedure, a large number of blank field realizations were constructed, in which the redshift was slightly displaced from the true value. This Monte Carlo technique is extremely powerful, providing an unbiased measure of the noise, including the systematic effects of continuum uncertainty, varying S/N among the quasars and within a single quasar spectrum, and contamination by unidentified absorption lines. Indeed, this last-named property allows a robust measure (§4) of the average column densities of ions lying in the Lyman alpha forest.

The measured distribution (solid line) of Si IV/C IV is compared with the average of

the random realizations (dashed line) in Figure 15 for all the systems, and also for those above and below $z = 3$. Si IV/C IV is clearly seen to be much stronger above $z = 3$. Figure 16 shows median Si IV/C IV values as a function of redshift, with errors derived from the distribution of medians in the blank-field realizations. The data again require a rapid jump at around $z = 3$, with values of 0.035 ± 0.005 below $z = 3$ and 0.10 ± 0.01 above.

4. Ionization Ratios

4.1. Introduction

The local shape of the ionizing flux and the value of the ionization parameter may be estimated from the relative distribution of the ionization levels of the various species. Most work to date has concentrated on using Si IV/C IV versus C II/C IV, which, as we have discussed in the introduction, is a powerful discriminant of the ionization parameter and of the strength of any break near the He⁺ edge. This diagnostic also relies on absorption lines that can be measured outside the forest. The Si IV/C IV versus C II/C IV method is reconsidered (§ 4.2) in the light of the present larger data set. However, the optical depth ratio method developed in §3.3 provides a powerful way to measure the average abundances of a number of other species (Si III, C III, N V, and O VI) that lie primarily within the Ly α forest. We use this technique in §4.3 to determine the ensemble properties of these ions as a function of redshift and to show that they can be fitted into a consistent interpretation of the evolution of the shape of the metagalactic flux.

4.2. Si IV/C IV versus C II/C IV

Si IV/C IV versus C II/C IV is shown in Figure 17 for the 29 complexes with $10^{13} \text{ cm}^{-2} < \text{N}(\text{C IV}) < 10^{14} \text{ cm}^{-2}$ and for which the C II line lies longward of the Ly α forest. Open squares denote systems with $z > 3$ and solid squares those with $z < 3$, while downward and/or leftward pointing arrows correspond to systems in which Si IV or C II is not detected, with the point positioned at the 1σ level. The curves show a range of models computed with the CLOUDY code (Ferland 1993) for a power-law ionizing spectrum with a range of breaks at the He⁺ edge at 4 Rydberg, and with $\log_{10}(\text{Si}/\text{C}) = -0.66$, typical of metal-poor systems. As was found previously in SC, while many of the low redshift systems are consistent with photoionization by a pure power law, most of the high redshift systems have Si IV/C IV values which are much too high relative to C II/C IV for this to be the case. They are consistent with photoionization by heavily broken power laws with breaks across the He⁺

edge in excess of 20 and softness ratios, $S \equiv f_\nu(4 \text{ Ryd})/f_\nu(1 \text{ Ryd})$ in excess of 300.

The models of SC were computed with simple broken power laws and a more extensive discussion of more general spectra may be found in Giroux & Shull (1997). However, Figure 18 illustrates that the general behaviour is fairly model invariant; it compares the data with a wide range of power laws (-1.5 to -2.5) again computed with $\log_{10}(\text{Si/C}) = -0.66$. Unless Si/C is made unreasonably high at $z > 3$, not even the softest power law spectrum (the top curve) can approach the high Si IV/C IV values. The introduction of the break at 4 Ryd moves the curves to a new asymptote, as is illustrated by the dashed and dotted curves. Both are computed with an ionization parameter of -1.6 and a -2 power law spectrum below 4 Ryd, but with a range of break strengths. The dotted curve corresponds to the same models as in Figure 17 in which the spectrum above the break is extrapolated with the same spectral index as it has below the break but at the lower flux level, as might be the case if there was a substantial galaxy contribution to the ionizing spectrum. The dashed line is computed instead with a model in which the break is a He^+ opacity whose cross section reduces as $E^{-2.7}$ at higher energies. This latter model asymptotes to the same Si IV/C IV values but requires a larger softness ratio of greater than about 2000 to achieve this. It is this effect that gave rise to Rauch et al.'s (1997) incorrect conclusion that He^+ breaks could not account for the high values of Si IV/C IV in high ionization systems since they used a recovering spectrum and an intermediate softness parameter (a flux reduction of 100 at 4 Ryd). However, as the break becomes large, both models reach the same limiting values which are consistent with the observed high values of Si IV/C IV and low values of C II/C IV.

In this asymptotic limit of a large break at the He^+ edge, the Si IV/C IV to C II/C IV ratio approaches a single track characterized essentially uniquely by the ionization parameter, which determines, modulo a very weak dependence on spectral index, the C II/C IV value. Therefore most of both the high and low redshift systems are consistent with a relatively small range of ionization parameter, $\log_{10} \Gamma = -1$ to -2 , but the higher redshift systems mostly require the high energy spectrum to be blocked above 54 eV whereas at the low redshifts this is not generally the case. It is perhaps important to emphasise that this effect is not observationally subtle and in Figure 19 we show C IV, Si IV and C II profiles for a sample of the high Si IV/C IV systems over the redshift range. For the high Si IV/C IV systems at low redshift, C II is generally clearly present but many of the high- z high Si IV/C IV systems are simply missing C II absorption.

4.3. Other ion ratios

The optical depth technique discussed in section 3 can also be used to determine the average properties of other important ions such as C III, Si III and O VI whose transitions lie below the wavelength of Ly α and for which individual line strengths cannot be reliably determined because of forest contamination.

As with Si IV, the value of $\tau(X)\lambda_X F_X/\tau(\text{C IV})\lambda_{\text{C IV}} f_{\text{C IV}}$ was determined for the ion, X , at all positions at which significant C IV absorption was present (again, $\tau(\text{C IV } 1550) > 0.05$) and a distribution of this quantity was constructed. A large number of random realizations were then made in which the C IV redshift was slightly displaced, to determine the backgrounds and errors. Because of forest contamination, which acts as an effective noise source, the errors are larger than for species that lie outside the forest, such as Si IV.

Figure 20 shows the distributions of C III/C IV, N V/C IV and O VI/C IV for all the available systems, and separately for $z > 3$ and $z < 3$ systems where the division is possible. The median and mean values and their 1σ errors for a range of ions are given in Tables 3 and 4 respectively. As is expected, O VI is strongly detected, with a median $N(\text{O VI})/N(\text{C IV}) = 1.97 \pm 0.28$. C III, Si III and N V are more weakly detected, with a median $N(\text{C III})/N(\text{C IV}) = 0.75 \pm 0.25$. Neither Si II nor C II is significantly detected.

The ionization patterns above and below $z = 3$ are summarised in Figure 21 which uses the more robust median values. The points show the quantities $A_C N(X)/A_X N(\text{C IV})$, where (A_X/A_C) is the assumed abundance of the element X with respect to C, which is taken to be $[\text{O}/\text{C}] = 0.5$, $[\text{Si}/\text{C}] = 0.4$ and $[\text{N}/\text{C}] = -0.7$, characteristic of low metallicity systems. This quantity is plotted against the ionization potential of the ion.

The primary difference between $z < 3$ and $z > 3$ remains the much higher abundance of Si IV at the higher redshift. The fractions of the high ions such as N V and O VI are marginally larger at $z < 3$ than at $z > 3$, but the effect is not large. The $z < 3$ ionization distribution can be reproduced quite well by a very simple model in which the ionizing spectrum is a -1.8 power law and $\Gamma = -1.6$; this is shown as the solid bars in Figure 21a. This highly oversimplified model is of course only a rough representation of the ensemble average of conditions in the IGM. However, for $z > 3$ we need a mix of conditions. As is discussed above, most of the systems must lie in the regions exposed to highly broken spectra in order to reproduce the lower ion ratios, particularly Si IV/C IV, but some fraction of the volume must still be ionized by spectra containing higher energy photons to reproduce the observed O VI, if this is assumed to be produced by photoionization. A model in which 70% of the systems are irradiated by a fully broken spectrum with $\alpha = -1.8$ below the break and $\Gamma = -1.5$, and 30% of the volume is occupied by a pure $\alpha = -1.8$ spectrum with $\Gamma = -1.0$

provides a reasonable representation, as is shown by the bars in Figure 21b.

5. Conclusions

I summarise the results of the paper by noting that, irrespective of the analysis methodology adopted, there is a significant change in the ionization balance of forest metal lines which occurs just below a redshift of 3. At lower redshifts, the ionization balance in the forest lines is fully consistent with a pure power law ionization spectrum with an index of -1.8 but at higher redshifts the high values of Si IV/C IV seen in most of the forest clouds despite generally low C II/C IV values implies that the ionizing flux must be very soft, with a large break at the He⁺ edge. The change occurs quite rapidly between $z = 2.9$ and $z = 3$, just above the redshift at which highly patchy He II Ly α absorption is seen in the quasar HE 2347–4342 (Reimers et al. 1997). The simplest explanation seems to be that we are seeing the redshift at which He II ionizes completely to He III as the He III Strömgen spheres overlap.

I am grateful to the many people at the Keck telescopes who assisted with these observations and most particularly to Steve Vogt whose HIRES spectrograph made them possible. I would also like to thank Len Cowie and Esther Hu for obtaining some of the observations on which this work is based, Dieter Reimers for computing positions and magnitudes for unpublished bright quasars, and Sandra Savaglio for providing updated information on higher redshift Si IV/C IV values. The research was supported by the National Science Foundation under grant AST 96-17216.

REFERENCES

- Boksenberg, A. 1998, Structure and Evolution of the IGM from QSO Absorption Line Systems, Proc. 13th IAP Colloquium, eds. P. Petitjean and S. Charlot, (Paris: Nouvelles Frontières), in press [astro-ph/9710258].
- Davidson, A. F., Kriss, G. A., & Zheng, W. 1996, *Nature*, 380, 47.
- Ferland, G. 1993, U. of Kentucky, Dept. of Physics & Astronomy Internal Report.
- Giroux, M. L., & Shull, J. M. 1997, *AJ*, 113, 1505.
- Haardt, F. & Madau, P. 1996, *ApJ*, 461, 20.
- Hogan, C. J., Anderson, S. F. & Rugers, M. H. 1997, *ApJ*, 113, 1495.
- Jakobsen, P. et al. 1994, *Nature* 370, 35.
- Madau, P. & Meiksin, A. 1994, *ApJ*, 433, L53.
- Miralda-Escudé, J., & Rees, M. J. 1993, *MNRAS*, 260, 617.
- Rauch, M., Haehnelt, M. G. & Steinmetz, M. 1997, *ApJ*, 481, 601.
- Reimers, D., Köhler, S., Wisotzki, L., Groote, D., Rodriguez-Pascual, P., & Wamsteker, W. 1997, *A&A*, 327, 890.
- Savaglio, S., Cristiani, S., D’Odorico, S., Fontana, A., Giallongo, E., & Molaro, P. 1997, *A&A*, 318, 347.
- Songaila, A., Hu, E. M. & Cowie, L. L. 1995, *Nature* 375, 124.
- Songaila, A., & Cowie, L. L. 1996, *AJ*, 112, 335 [SC].
- Zheng, W., Davidson, A. F., & Kriss, G. A. 1998, *AJ*, in press.

Table 1. Observations

Quasar	Mag.	Expo. (hrs)	S/N	Complete	z_{low} (Si IV)	z_{low} (C II)	z_{high}
0014+813	16.5	7.65	120	Yes	2.81	3.00	3.31
0256–000	18.2	5.33	60	Yes	2.78	2.97	3.28
0302–003	17.8	10.67	90	Yes	2.72	2.91	3.21
0636+680	16.5	6.08	130	Yes	2.62	2.80	3.10
0741+4741	16.1	4.0	145	No	2.66	2.84	3.15
0956+122	17.5	6.67	90	Yes	2.74	2.92	3.23
1159+123	17.5	8.0	85	Yes	2.90	3.09	3.42
1422+231	16.5	9.3	330	Yes	3.01	3.21	3.54
1623+269	16.0	3.33	60	Yes	2.12	2.27	2.48
1700+6416	16.1	8.33	260	Yes	2.27	2.43	2.68
2000–330	19.0	4.67	60	Near	3.14	3.36	3.69
2126–158	17.3	4.45	130	No	2.72	2.90	3.21
2347–4342	16.3	6.67	130	Yes	2.37	2.54	2.82

Table 2. C IV, Si IV, C II and Si II Column Densities

Quasar	z	# cpts.	$N(\text{C IV})$	$N(\text{Si IV})$	$N(\text{C II})$	$N(\text{Si II})$
1623+269	2.16141	3	6.1×10^{13}	1.4×10^{12}	...	-1.9×10^{11}
1623+269	2.24450	2	3.1×10^{13}	-3.2×10^{10}	...	-2.4×10^{11}
1700+6416	2.28952	2	6.8×10^{12}	6.2×10^{10}	...	-2.6×10^{11}
1700+6416	2.30826	3	3.4×10^{13}	1.7×10^{12}	...	-9.5×10^{11}
1700+6416	2.31536	13	1.9×10^{15}	6.1×10^{13}	...	9.5×10^{12}
1700+6416	2.37984	2	1.3×10^{13}	7.3×10^{11}	...	4.6×10^{11}
1623+269	2.40085	5	1.2×10^{14}	-1.8×10^{11}	9.7×10^{10}	4.5×10^{11}
1700+6416	2.43304	7	4.3×10^{13}	9.0×10^{12}	...	-1.2×10^{11}
2347-4342	2.43814	2	7.5×10^{12}	3.0×10^{11}	...	-3.4×10^{10}
1700+6416	2.43863	8	5.2×10^{13}	2.0×10^{12}	2.6×10^{11}	-1.3×10^{12}
1623+269	2.44353	3	1.7×10^{13}	6.8×10^{10}	-3.1×10^{12}	-1.2×10^{12}
1623+269	2.44534	2	6.3×10^{12}	1.0×10^{12}	2.7×10^{12}	1.4×10^{10}
1700+6416	2.56817	2	6.6×10^{12}	2.6×10^{11}	-5.5×10^{10}	2.0×10^{10}
1700+6416	2.57857	4	3.6×10^{13}	1.3×10^{12}	1.9×10^{12}	-3.6×10^{11}
2347-4342	2.63449	2	9.9×10^{12}	1.8×10^{10}	9.9×10^{12}	-3.0×10^{11}
0741+4741	2.67283	2	1.0×10^{13}	8.7×10^{10}	...	1.3×10^{11}
0636+680	2.68228	2	8.4×10^{12}	7.8×10^{11}	...	1.0×10^{12}
0741+4741	2.69235	2	6.5×10^{13}	4.0×10^{12}	...	-2.7×10^{11}
0741+4741	2.69478	2	2.7×10^{13}	6.8×10^{11}	...	-5.5×10^{11}
0741+4741	2.71446	2	6.3×10^{12}	2.8×10^{11}	...	1.9×10^{11}
2126-158	2.72796	3	2.8×10^{13}	2.3×10^{12}	...	-6.1×10^{11}
0741+4741	2.73323	2	5.1×10^{13}	5.3×10^{12}	...	-1.1×10^{12}
2347-4342	2.73564	5	1.1×10^{14}	1.9×10^{13}	6.8×10^{12}	4.8×10^{10}
2126-158	2.76916	12	4.6×10^{14}	6.4×10^{13}	...	6.5×10^{14}
0741+4741	2.78488	2	1.0×10^{13}	3.9×10^{11}	...	-1.6×10^{11}
0302-003	2.78663	9	7.1×10^{13}	3.1×10^{12}	...	4.9×10^{11}
2126-158	2.81959	5	3.0×10^{13}	2.0×10^{12}	...	1.7×10^{11}
0256-000	2.82444	6	2.3×10^{13}	1.2×10^{12}	...	-7.1×10^{11}
0302-003	2.82593	2	6.8×10^{12}	-2.4×10^{11}	...	2.1×10^{11}
0956+122	2.83185	2	1.3×10^{13}	8.3×10^{10}	...	-6.9×10^{11}
0956+122	2.83433	2	8.9×10^{12}	2.3×10^{11}	...	-2.1×10^{11}
0256-000	2.83599	2	5.6×10^{12}	4.2×10^{11}	...	8.0×10^{11}
0636+680	2.86883	2	7.3×10^{12}	5.0×10^{11}	-3.9×10^{11}	4.7×10^{11}
0956+122	2.88806	4	1.3×10^{13}	5.1×10^{11}	...	1.1×10^{12}

Table 2—Continued

Quasar	z	# cpts.	$N(\text{C IV})$	$N(\text{Si IV})$	$N(\text{C II})$	$N(\text{Si II})$
0636+680	2.89163	5	2.8×10^{13}	5.6×10^{10}	4.5×10^9	-6.6×10^{11}
0636+680	2.90374	9	3.0×10^{14}	1.4×10^{14}	4.3×10^{14}	5.5×10^{13}
0741+4741	2.90455	6	2.4×10^{13}	7.8×10^{11}	2.2×10^{12}	-1.4×10^{12}
2126-158	2.90708	2	3.6×10^{13}	8.7×10^{12}	5.5×10^{12}	-3.1×10^{11}
0014+813	2.90823	2	6.8×10^{12}	4.5×10^{11}	...	6.5×10^{11}
0956+122	2.91490	2	8.7×10^{12}	2.1×10^{11}	...	-3.4×10^8
0302-003	2.91749	2	1.8×10^{13}	5.0×10^{11}	1.3×10^{12}	4.0×10^{11}
0302-003	2.95882	2	7.2×10^{12}	1.1×10^{11}	-1.1×10^{12}	-3.5×10^{11}
2126-158	2.96346	3	2.0×10^{13}	5.5×10^{12}	1.6×10^{11}	9.8×10^{11}
0741+4741	2.96530	3	1.0×10^{13}	-1.3×10^{11}	2.6×10^{11}	6.7×10^{11}
2126-158	2.96747	5	2.5×10^{13}	3.8×10^{12}	9.1×10^{12}	7.0×10^{11}
0302-003	2.99540	2	6.6×10^{12}	3.2×10^{11}	-1.9×10^{12}	-2.4×10^{11}
0302-003	3.00295	2	3.3×10^{13}	1.7×10^{12}	7.4×10^{11}	1.2×10^{12}
0956+122	3.01043	2	9.7×10^{12}	1.5×10^{12}	3.8×10^{12}	-1.0×10^{12}
0636+680	3.01303	2	1.3×10^{13}	5.8×10^{11}	-1.4×10^{12}	-7.8×10^{11}
0636+680	3.01749	2	4.1×10^{13}	1.2×10^{12}	7.0×10^{11}	-4.1×10^9
0741+4741	3.01763	6	6.6×10^{13}	2.5×10^{13}	1.1×10^{15}	1.5×10^{14}
0256-000	3.01799	2	1.5×10^{13}	1.7×10^{12}	4.3×10^{10}	-1.2×10^{12}
0741+4741	3.03469	3	1.0×10^{13}	9.7×10^{11}	5.9×10^{10}	-2.3×10^{11}
0302-003	3.04705	2	5.7×10^{12}	-8.7×10^{10}	3.2×10^{11}	-5.7×10^{10}
0956+122	3.05287	2	1.0×10^{13}	1.8×10^{12}	-3.3×10^{11}	6.1×10^{10}
0741+4741	3.05366	4	1.1×10^{13}	6.3×10^{12}	-1.7×10^{12}	1.7×10^{11}
0256-000	3.08434	2	4.5×10^{13}	1.3×10^{13}	6.6×10^{12}	1.7×10^{11}
1422+231	3.09030	4	4.2×10^{13}	3.1×10^{12}	...	-1.3×10^{11}
0956+122	3.09691	2	7.1×10^{12}	1.0×10^{12}	1.5×10^{12}	8.6×10^{11}
0956+122	3.11418	2	6.9×10^{13}	3.9×10^{12}	1.2×10^{12}	-5.2×10^{11}
1422+231	3.13413	3	1.6×10^{13}	9.7×10^{11}	...	-3.3×10^{10}
1422+231	3.13702	2	6.2×10^{12}	1.1×10^{12}	...	5.3×10^{11}
0956+122	3.15294	5	3.9×10^{13}	1.2×10^{13}	4.2×10^{12}	3.3×10^{11}
1159+123	3.16701	2	8.6×10^{12}	5.5×10^{11}	-3.6×10^{11}	1.5×10^{11}
2000-330	3.17249	2	1.3×10^{13}	6.7×10^{12}	...	2.1×10^{12}
0956+122	3.17860	3	1.6×10^{13}	2.3×10^{12}	8.8×10^{11}	-3.0×10^{11}
2000-330	3.19155	5	7.6×10^{13}	1.9×10^{13}	...	6.2×10^{13}
0256-000	3.19849	2	1.6×10^{13}	2.4×10^{11}	6.3×10^{11}	2.6×10^{11}

Table 2—Continued

Quasar	z	# cpts.	$N(\text{C IV})$	$N(\text{Si IV})$	$N(\text{C II})$	$N(\text{Si II})$
0956+122	3.22310	5	7.5×10^{13}	1.5×10^{13}	2.0×10^{12}	1.9×10^{11}
1159+123	3.22554	2	2.6×10^{13}	2.2×10^{12}	-1.3×10^{12}	-2.7×10^{11}
0014+813	3.22623	5	5.8×10^{13}	3.0×10^{12}	-1.6×10^{12}	-1.3×10^{12}
0014+813	3.23339	2	9.6×10^{12}	1.0×10^{12}	2.0×10^{11}	7.0×10^{10}
1159+123	3.26101	2	3.8×10^{13}	2.6×10^{12}	-4.0×10^{11}	7.6×10^{11}
2000-330	3.33281	4	6.2×10^{13}	2.9×10^{13}	...	3.8×10^{12}
2000-330	3.33714	2	2.7×10^{13}	3.7×10^{12}	...	8.2×10^{11}
1159+123	3.37844	2	1.6×10^{13}	2.2×10^{12}	1.3×10^{11}	-5.2×10^9
1422+231	3.38277	5	4.4×10^{13}	2.8×10^{12}	2.1×10^{12}	3.7×10^{11}
1159+123	3.40448	2	1.9×10^{13}	2.3×10^{12}	-6.8×10^{11}	3.5×10^{11}
1422+231	3.41121	2	8.7×10^{12}	1.7×10^{12}	4.7×10^{10}	7.9×10^{10}
1422+231	3.44717	2	4.0×10^{13}	7.6×10^{12}	-4.0×10^{10}	3.9×10^{10}
2000-330	3.50532	2	9.7×10^{12}	4.1×10^{12}	2.6×10^{12}	2.3×10^{10}
1422+231	3.53863	11	1.8×10^{14}	3.8×10^{13}	4.4×10^{13}	2.4×10^{12}
2000-330	3.54937	11	2.3×10^{14}	6.3×10^{13}	1.7×10^{14}	9.4×10^{12}

Table 3. Medians of Column Density Ratios With Respect to C IV

Ion	All	$z > 3$	$z < 3$
C II	0.02 ± 0.03	0.01 ± 0.04	0.03 ± 0.09
C III	...	0.75 ± 0.25	...
C IV	1	1	1
Si II	-0.001 ± 0.004	0.004 ± 0.010	-0.004 ± 0.006
Si III	0.029 ± 0.010	0.08 ± 0.037	0.013 ± 0.019
Si IV	0.056 ± 0.003	0.10 ± 0.005	0.035 ± 0.004
N V	0.019 ± 0.008	0.018 ± 0.024	0.019 ± 0.006
O VI	1.97 ± 0.28	1.59 ± 0.21	2.75 ± 0.78

Table 4. Means of Column Density Ratios With Respect to C IV

Ion	All	$z > 3$	$z < 3$
C II	−0.28	−0.03	−0.47
C III	...	1.97	...
C IV	1	1	1
Si II	0.08	0.27	−0.07
Si III	0.0	0.07	−0.04
Si IV	0.12	0.17	0.07
N V	0.05	0.09	0.02
O VI	1.8	1.3	2.2

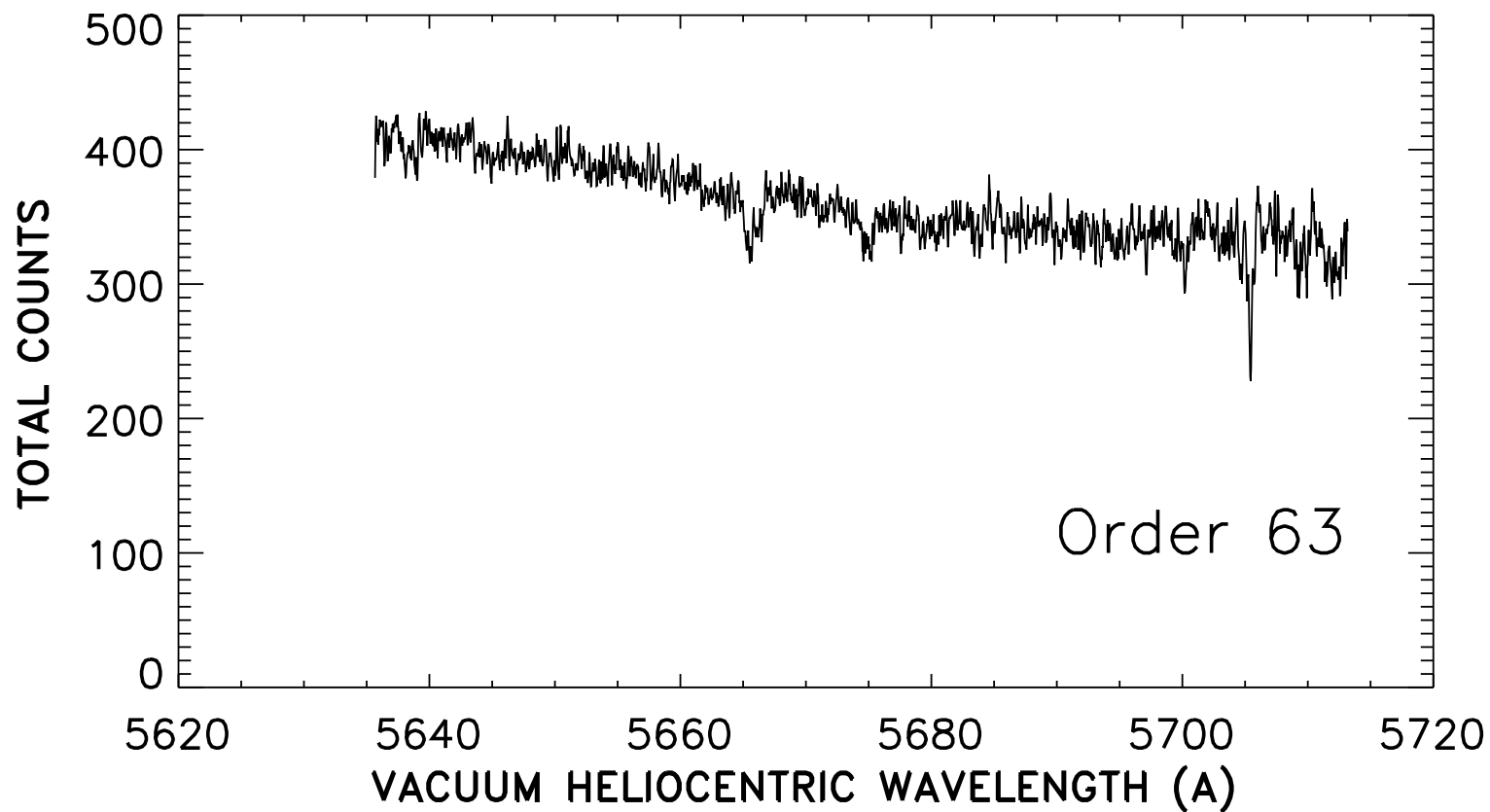


Fig. 1a.— A sample extraction of one of the orders longward of the Ly α forest in the quasar Q1159+123. The total exposure is 2 hr, consisting of three 40 m integrations. The spectrum is unsmoothed and oversamples the resolution element.

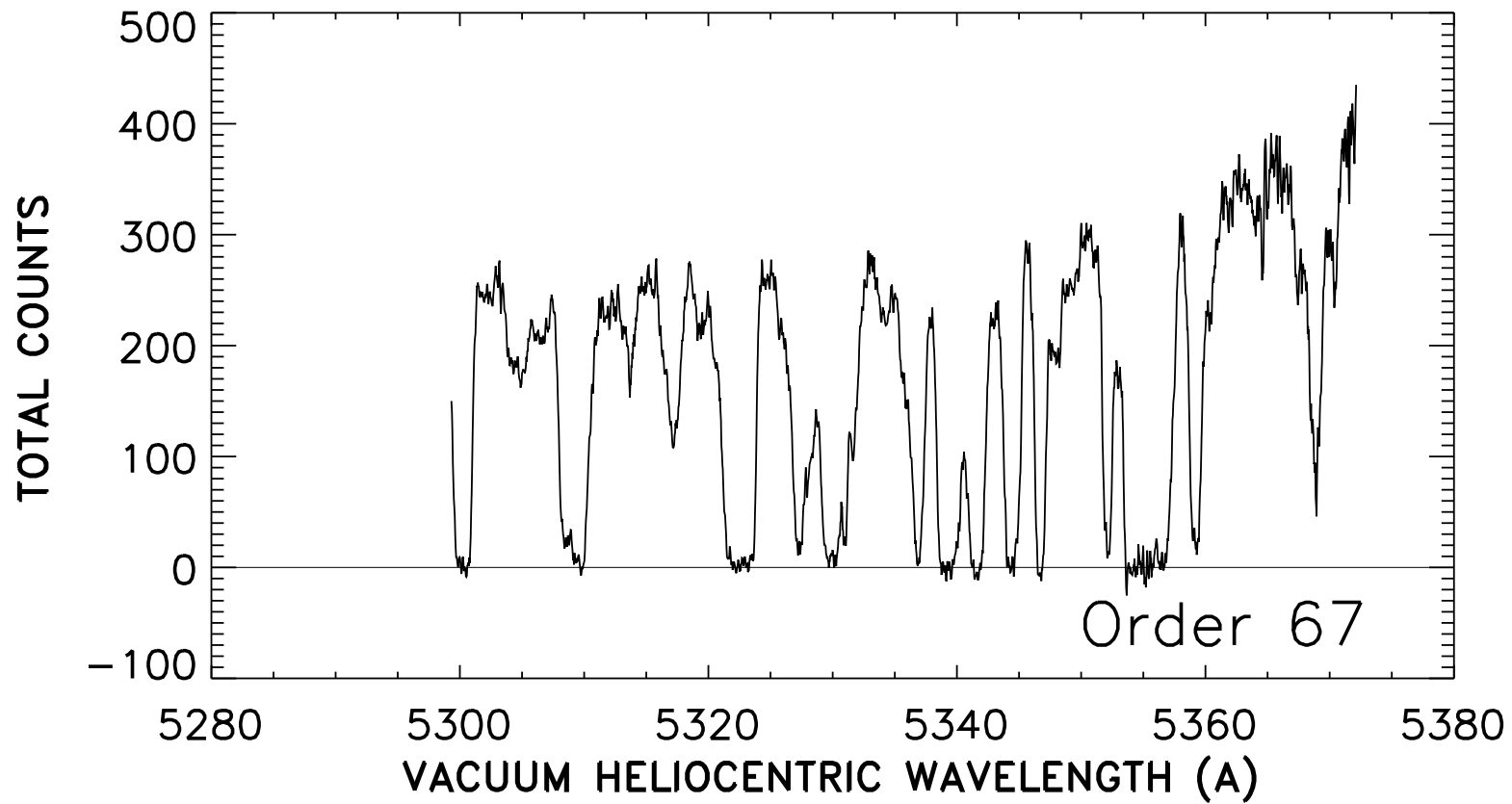


Fig. 1b.— An order in the same spectrum as (a) but lying in the Ly α forest. The precision of the sky subtraction may be assessed from the degree to which the bases of the saturated Ly α lines approximate to zero.

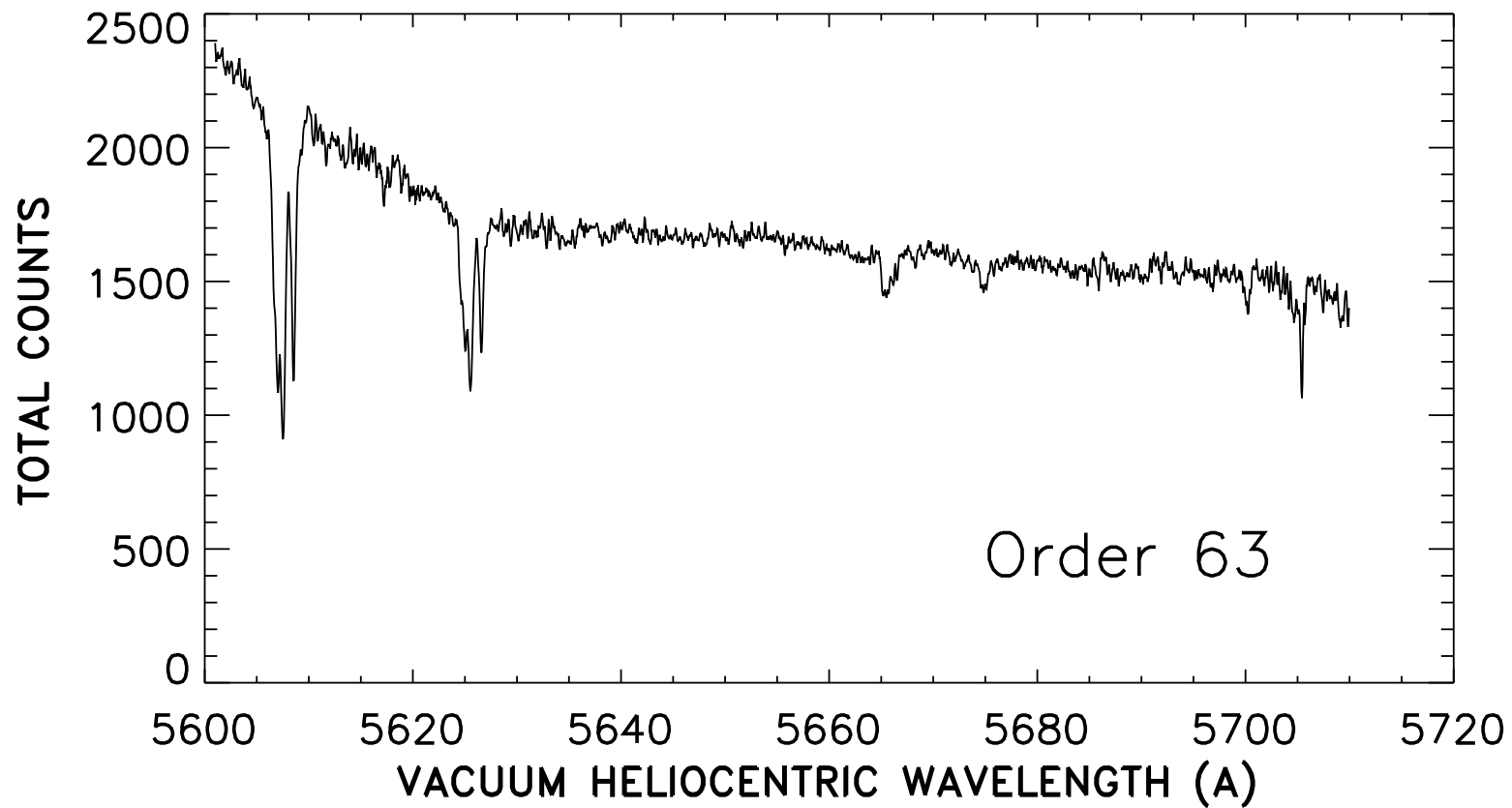


Fig. 2.— Final processed and extracted order in Q1159+123 for comparison with Figure 1(a). The total exposure of 8 hr is combined from a number of sub-exposures with spectra covering each order added in a S/N optimized fashion.

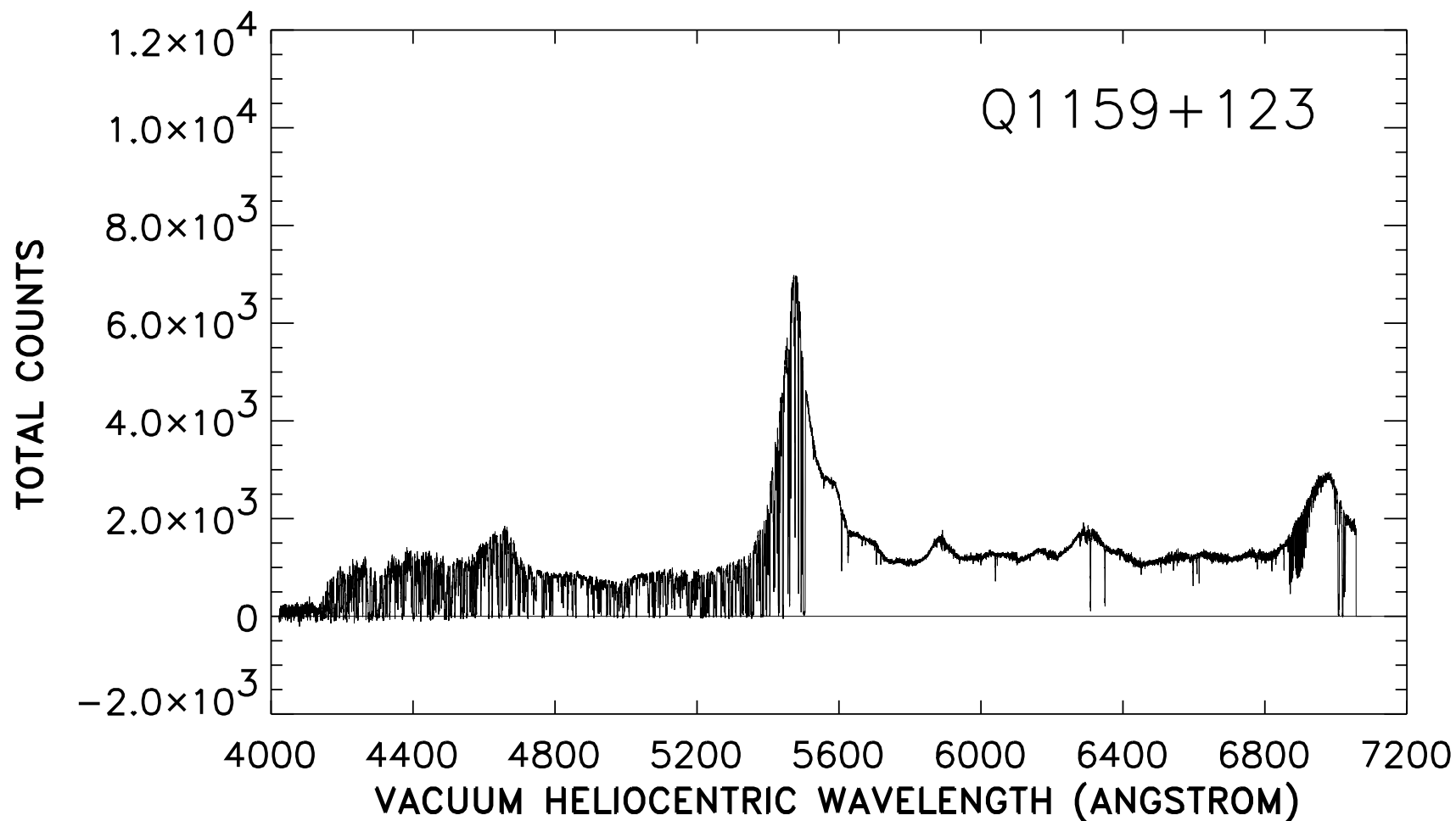


Fig. 3.— Complete spectrum of Q1159+123 formed by interpolating all the extracted orders to a uniform 0.05 \AA wavelength scale and then splicing adjacent orders. The principal feature is the quasar's Ly α emission near 5400 \AA and the spectrum extends just past C IV emission near 7000 \AA . There is a Lyman limit system near 4150 \AA . Most of the features longward of the Ly α emission are C IV doublets, except for the atmospheric A band.

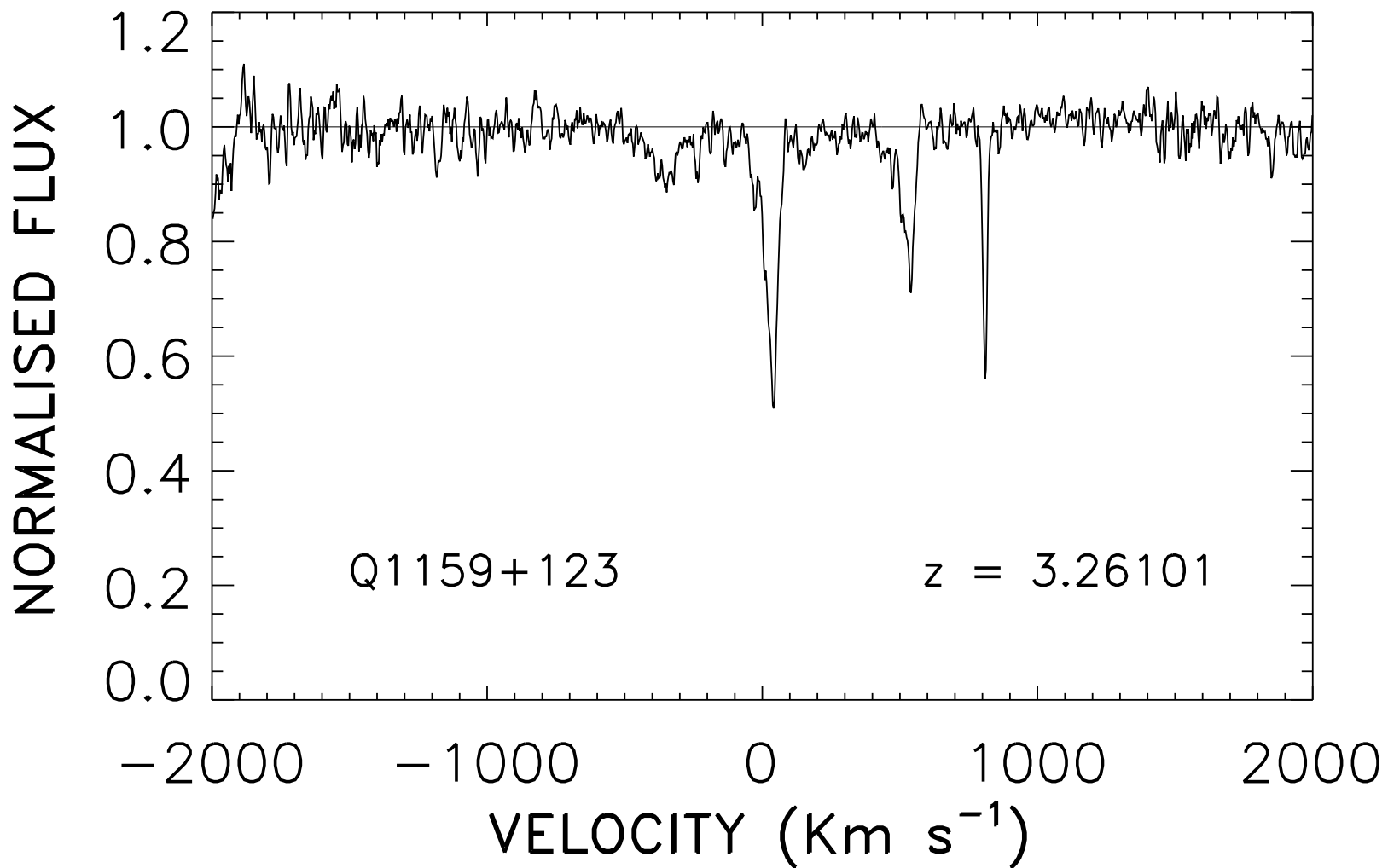


Fig. 4.— A typical continuum-fitted region of spectrum, around the $z = 3.26101$ C IV absorption line complex in Q1159+123. The continuum was fitted to a ± 2000 km s⁻¹ region around the C IV $\lambda 1548$ Å line by iterating a 2nd-order polynomial fit to a 10-pt smoothed spectrum and rejecting significantly deviant regions.

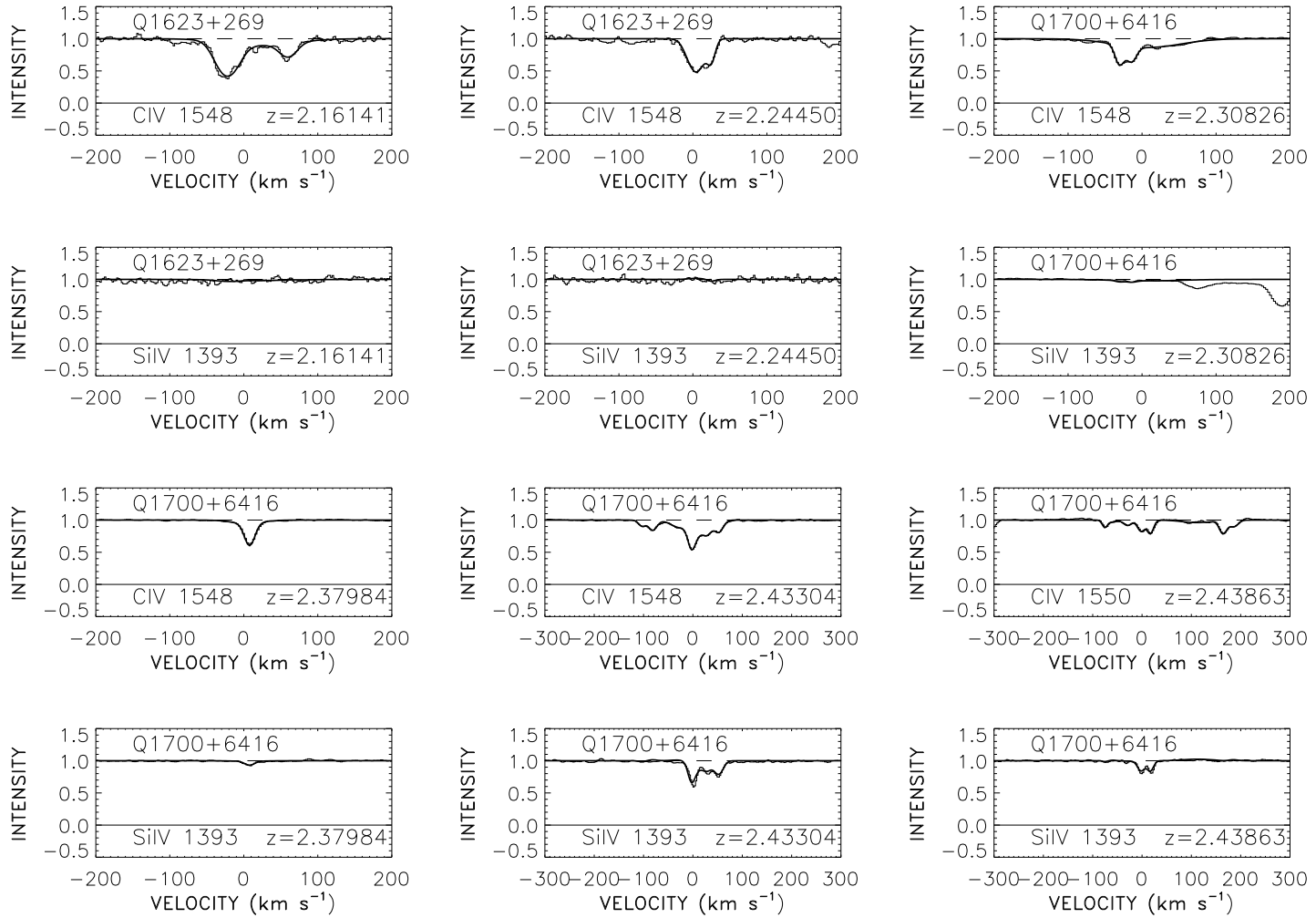


Fig. 5a-i.— Voigt profile fits to the C IV and Si IV doublets in all cloud complexes in the sample with $10^{13} \text{ cm}^{-2} < N(\text{C IV}) < 10^{14} \text{ cm}^{-2}$. All doublets lie redward of the quasar’s Ly α emission. Table 2 summarises the redshifts, number of Voigt components, total C IV and Si IV column densities of each complex, and C II and Si II column densities.

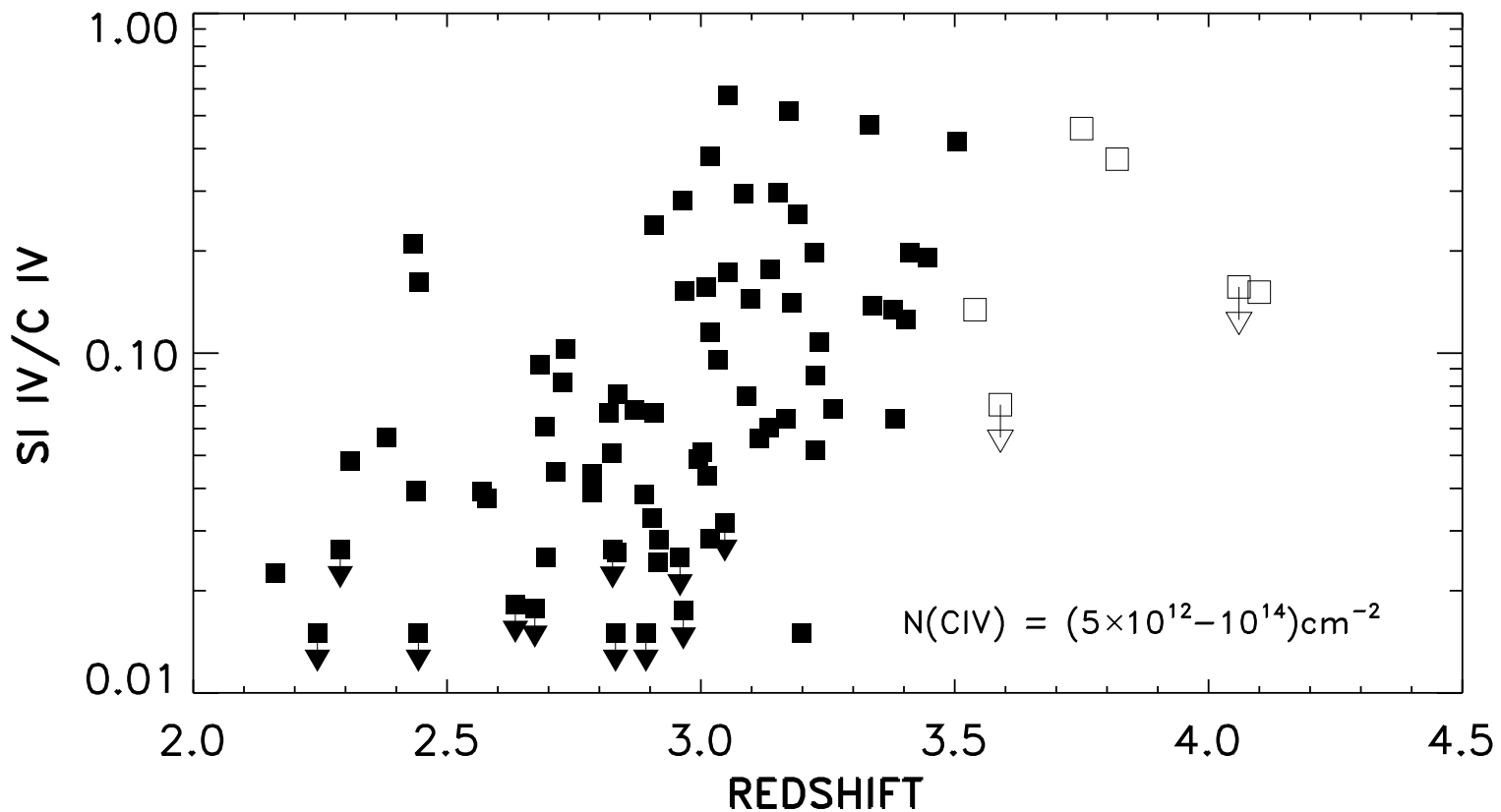


Fig. 6.— The ratio of total Si IV column density to total C IV column density as a function of redshift for the 76 complexes with $5 \times 10^{12} \text{ cm}^{-2} \leq N(\text{C IV}) \leq 10^{14} \text{ cm}^{-2}$ (filled squares). Open squares denote values from Savaglio et al.'s (1997) observations of Q0000–263. Downward pointing arrows show systems in which Si IV is not detected and where the points are positioned at the 1σ upper limit.

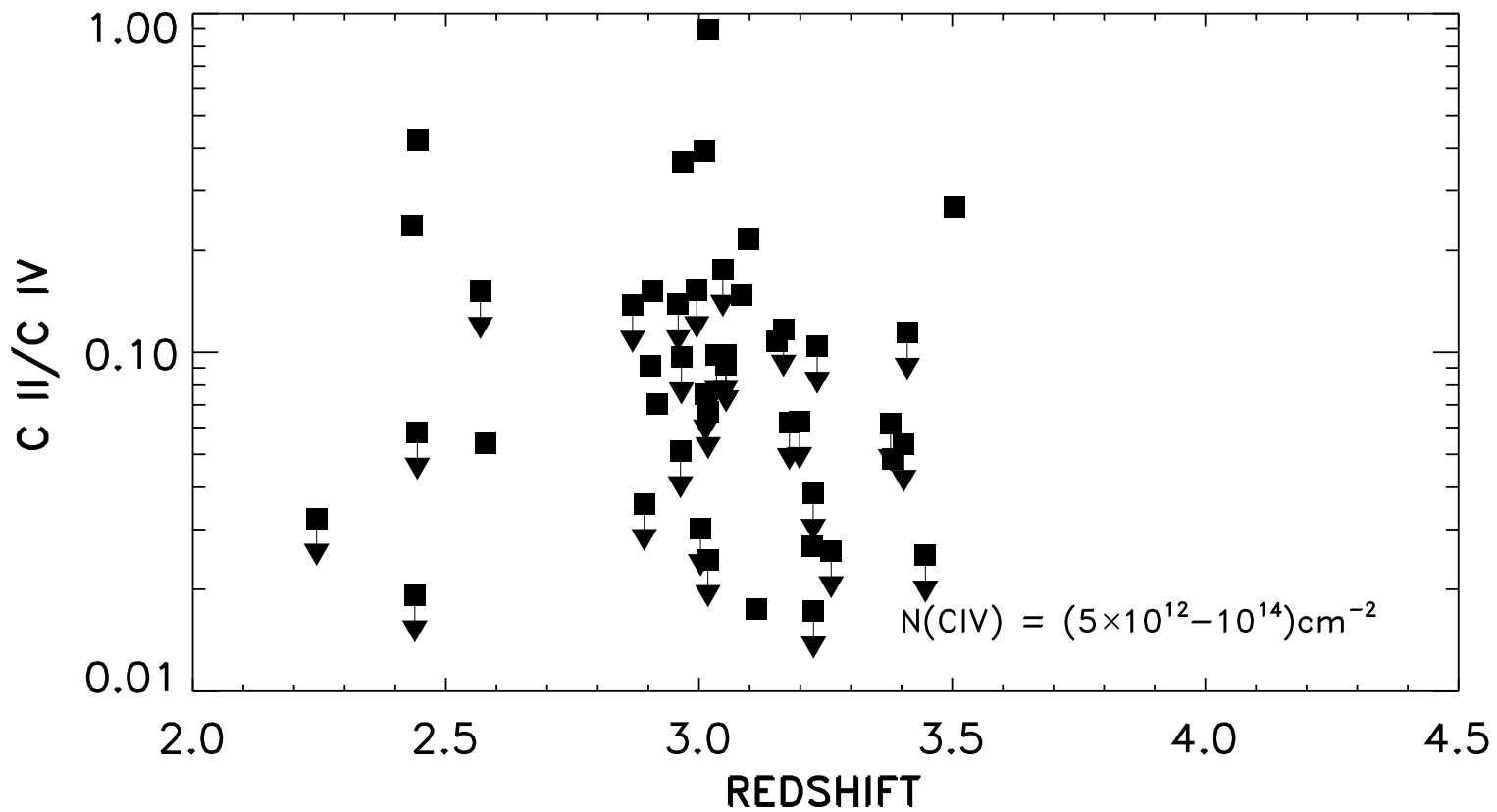


Fig. 7.— The ratio of total C II column density to total C IV column density as a function of redshift for the complexes of Figure 6 in which the C II system lies longer in wavelength than the forest. Downward pointing arrows show systems in which C II is not detected and where the points are positioned at the 1σ upper limit.

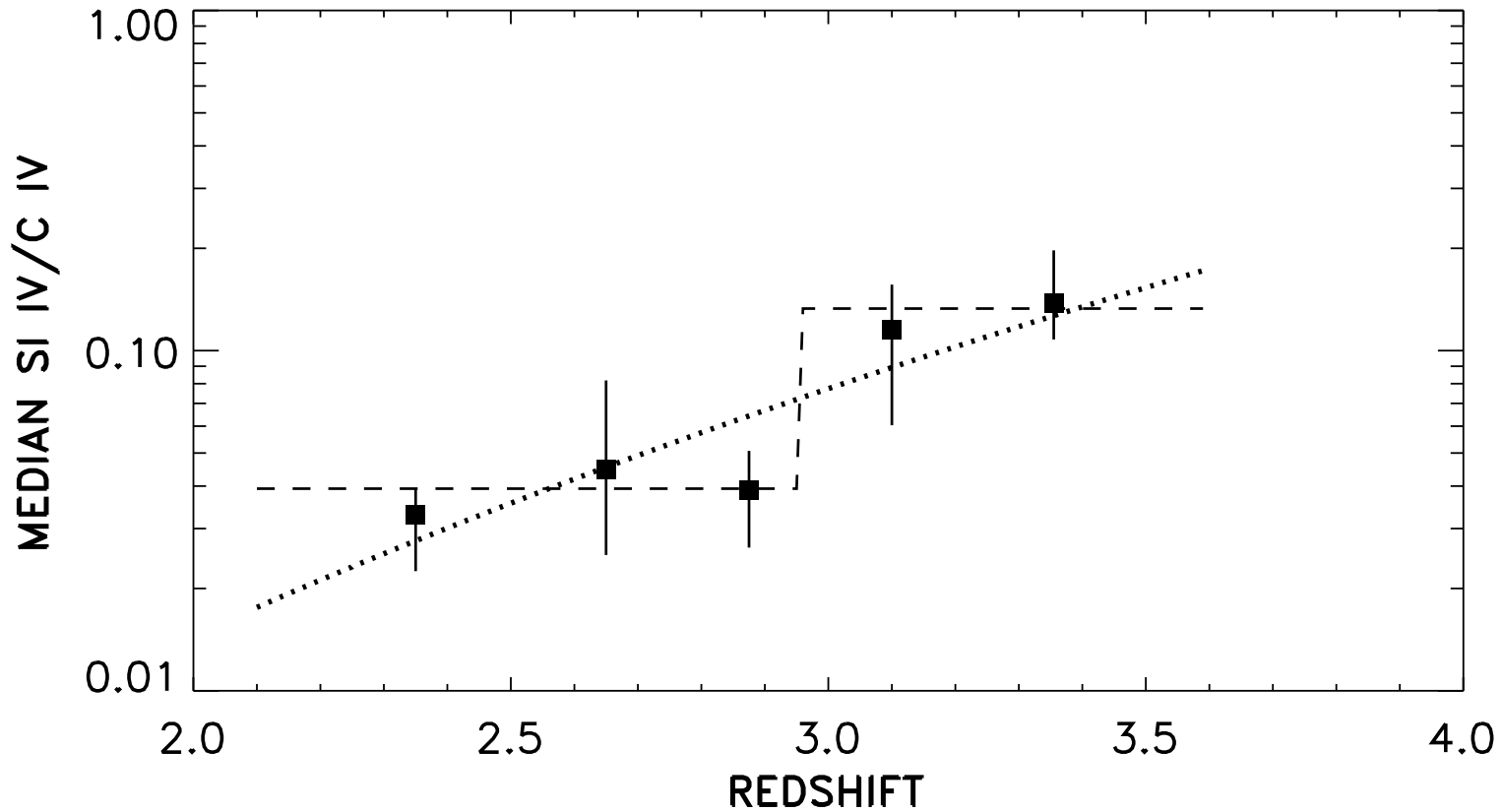


Fig. 8.— Median values of Si IV/C IV as a function of redshift for the sample of Figure 6. Errors are $\pm 1 \sigma$ computed using the median sign method. The median value of Si IV/C IV is $0.039^{+0.009}_{-0.006}$ for $z < 3$ and $0.13^{+0.04}_{-0.04}$ for $z > 3$. The dashed line is a step function fit to the data, with a jump of a factor of 3.4 at $z = 2.95$. The dotted line has the form $(1+z)^{5.4}$. It does not predict a sufficient jump between $z = 2.85$ and $z = 3.1$ to reconcile the low and high redshift distributions (Figure 9).

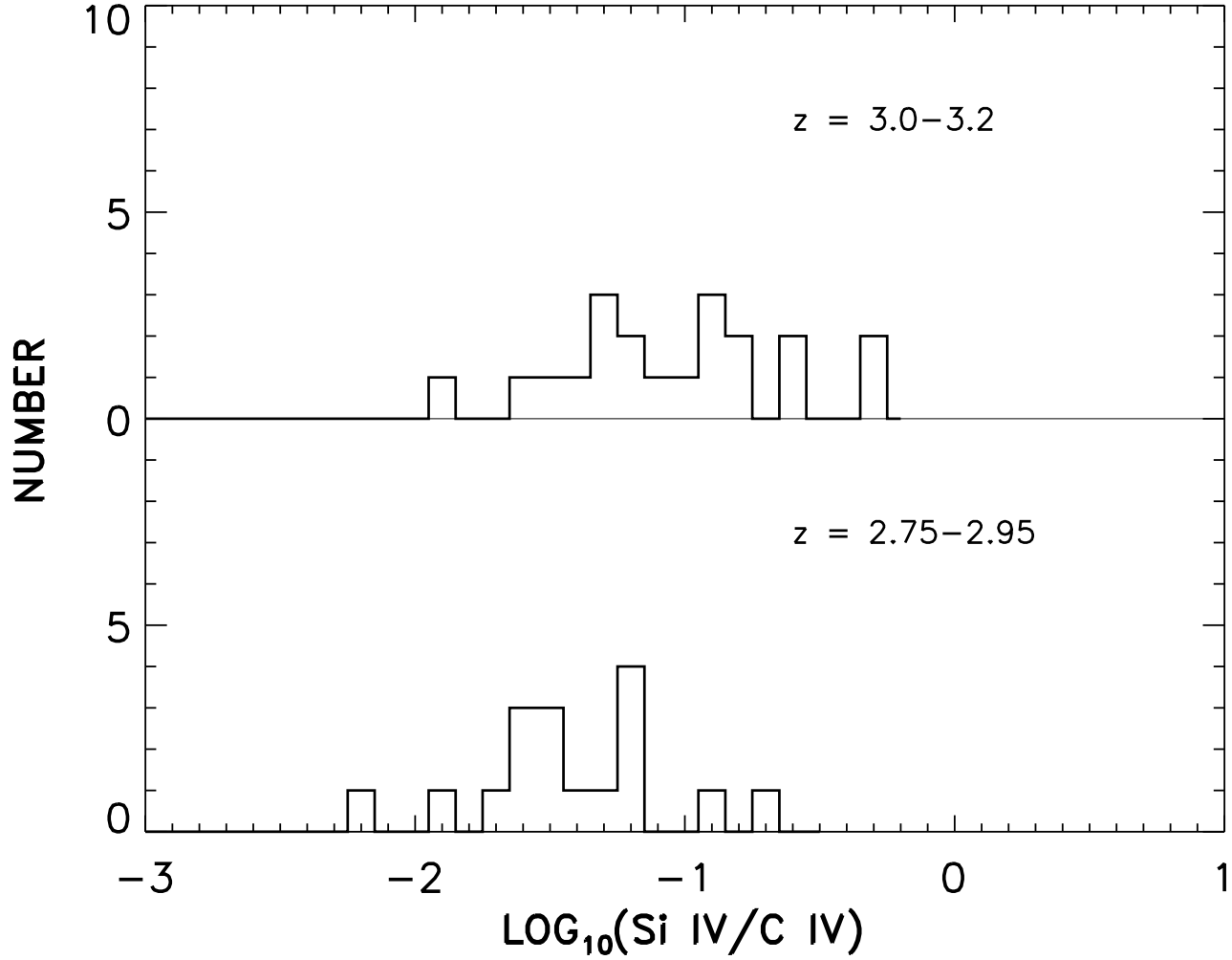


Fig. 9.— Histograms of the distributions of $\log_{10}(\text{Si IV}/\text{C IV})$ for 22 systems with $z = 3.0 - 3.2$ (top) with a median of $0.14^{+0.04}_{-0.075}$ and 16 systems with $z = 2.75 - 2.95$ (bottom) with a median of $0.038^{+0.029}_{-0.010}$. A multiplicative jump of a least a factor of 1.8 is required at the 98% confidence level to reconcile the low and high redshift distributions.

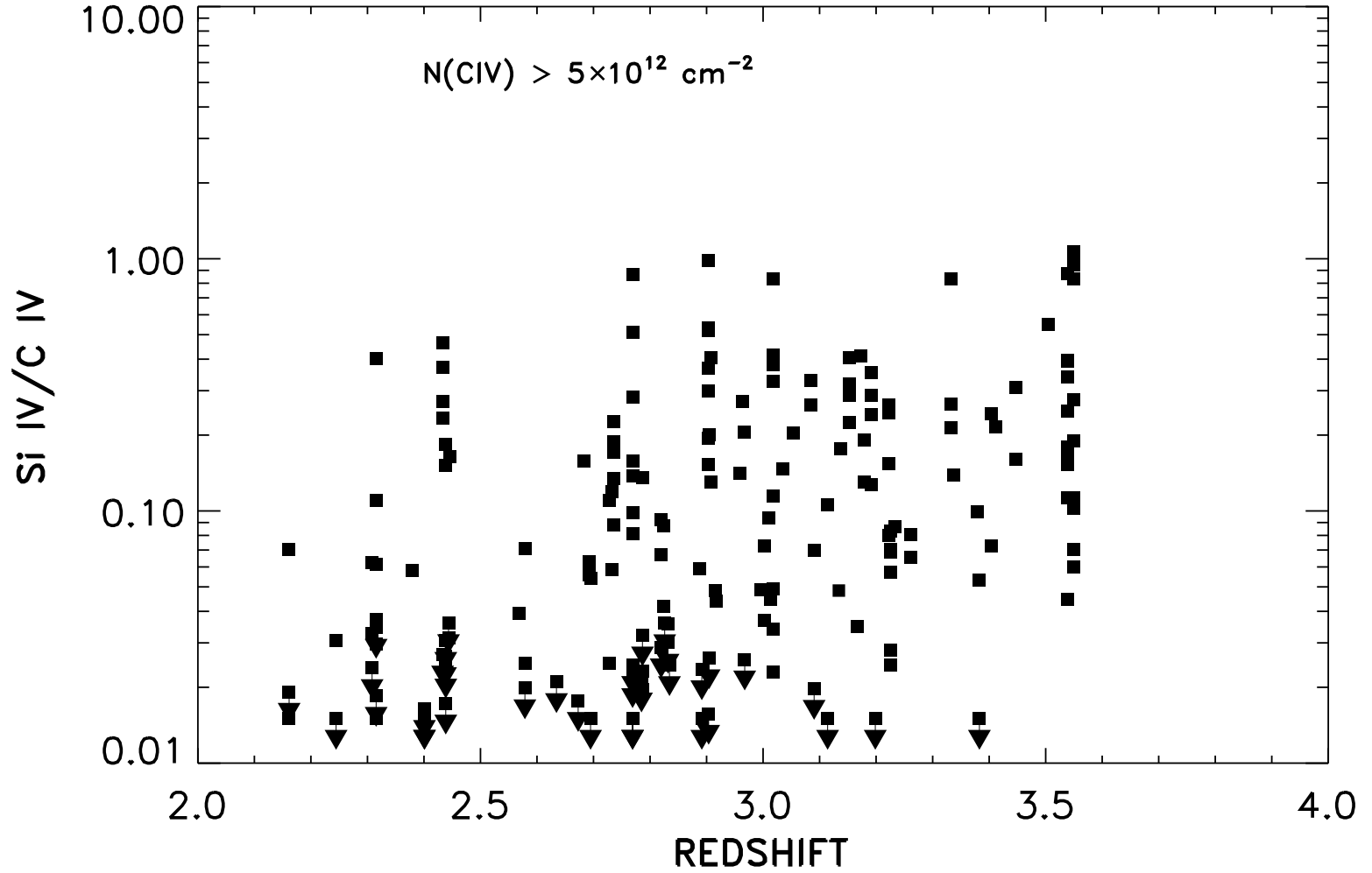


Fig. 10.— Si IV/C IV as a function of redshift for all Voigt profile components with $N(\text{C IV}) > 5 \times 10^{12} \text{ cm}^{-2}$ in the sample, irrespective of the total column density of the complex, and including a number of Lyman limit systems.

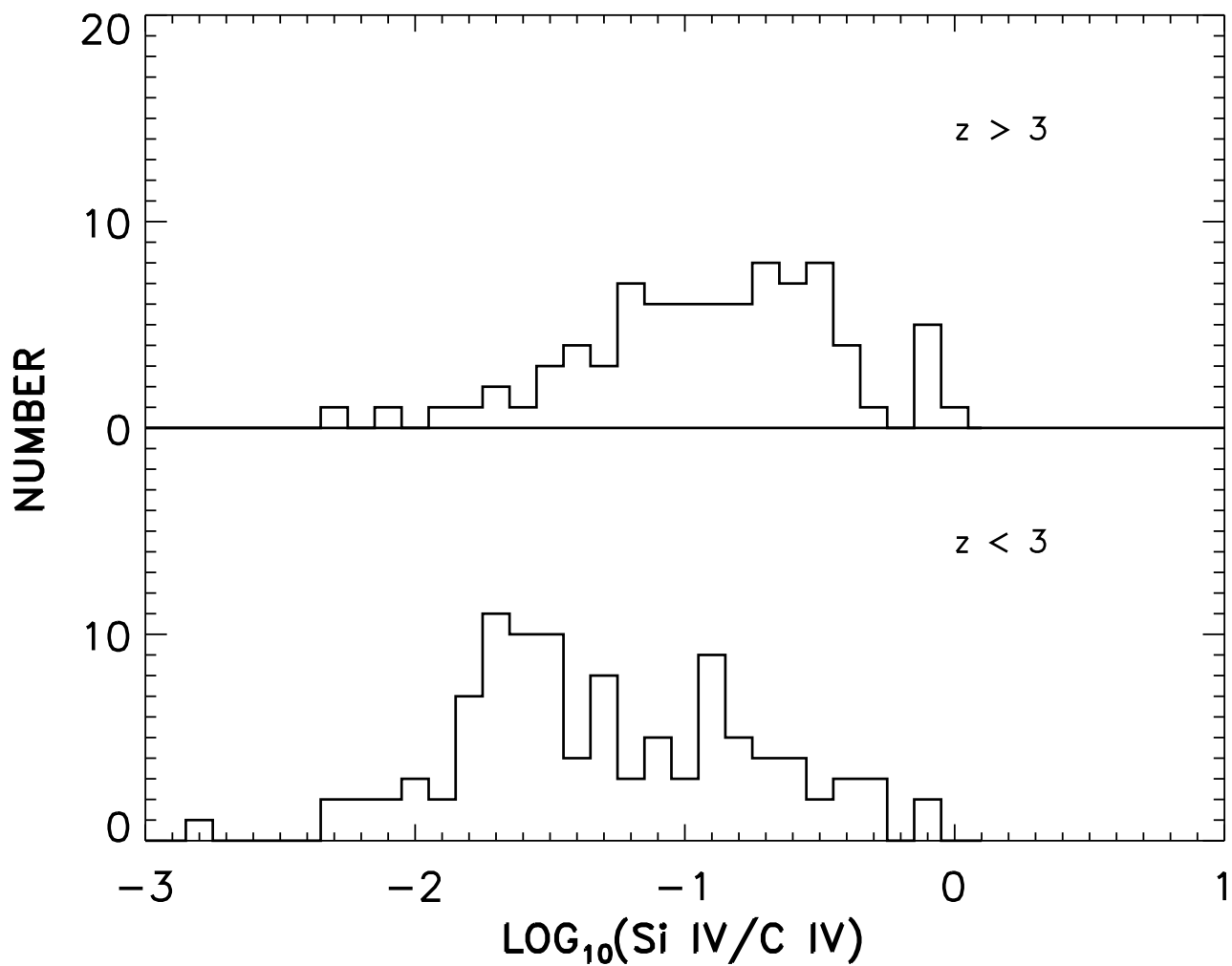


Fig. 11.— Histograms of the distributions of $\log_{10}(\text{Si IV}/\text{C IV})$ for all Voigt profile components in the sample of Figure 10 with $z > 3$ (top) with a median of $0.15^{+0.04}_{-0.04}$ and for $z < 3$ (bottom) with a median of $0.043^{+0.015}_{-0.008}$. A multiplicative jump of a least a factor of 1.93 is required at the 98% confidence level to reconcile the low and high redshift distributions.

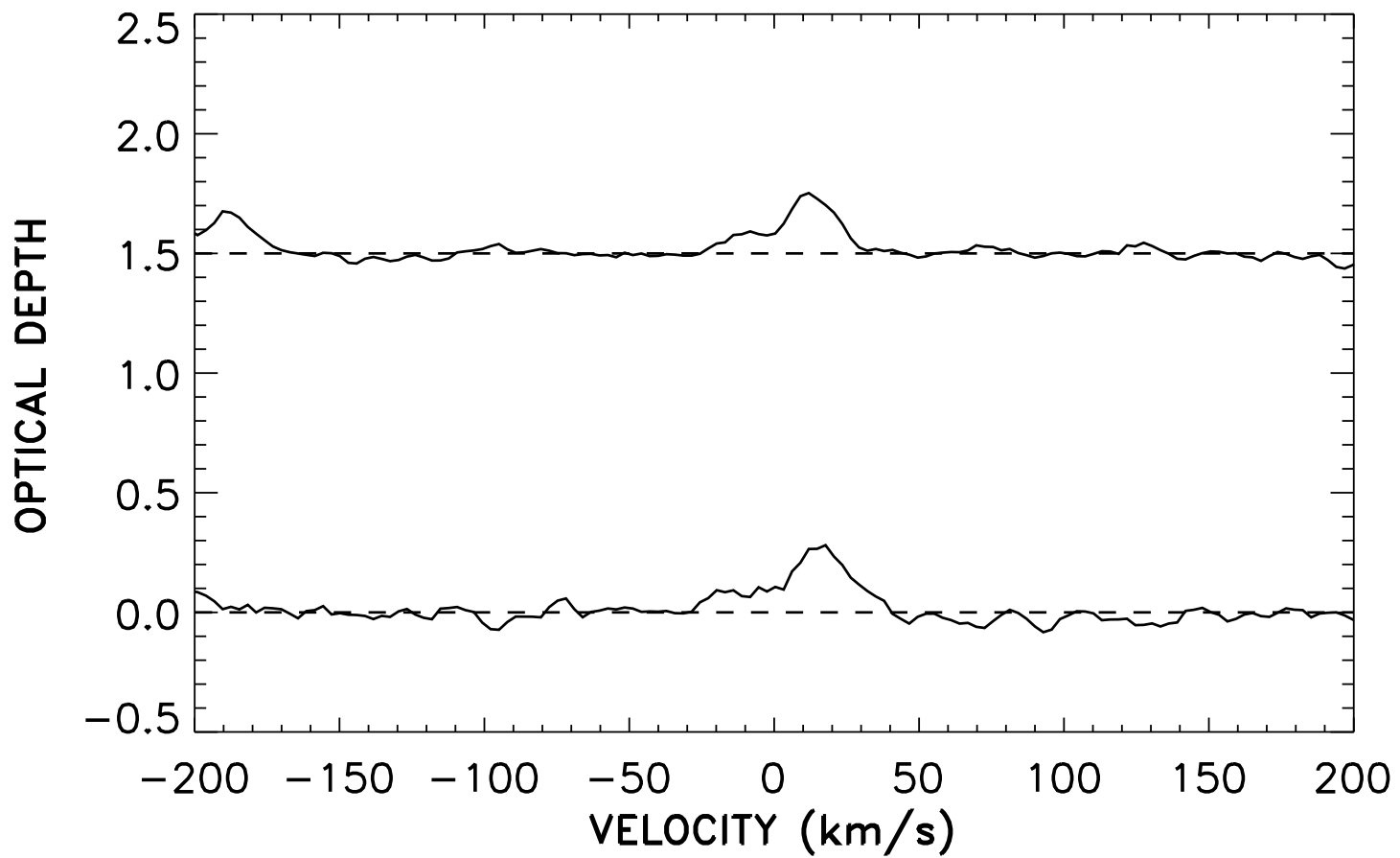


Fig. 12.— Sample optical depths of Si IV (top) and C IV (bottom) for the $z = 3.33714$ complex in Q2000–330. The Si IV optical depth has been offset by 1.5.

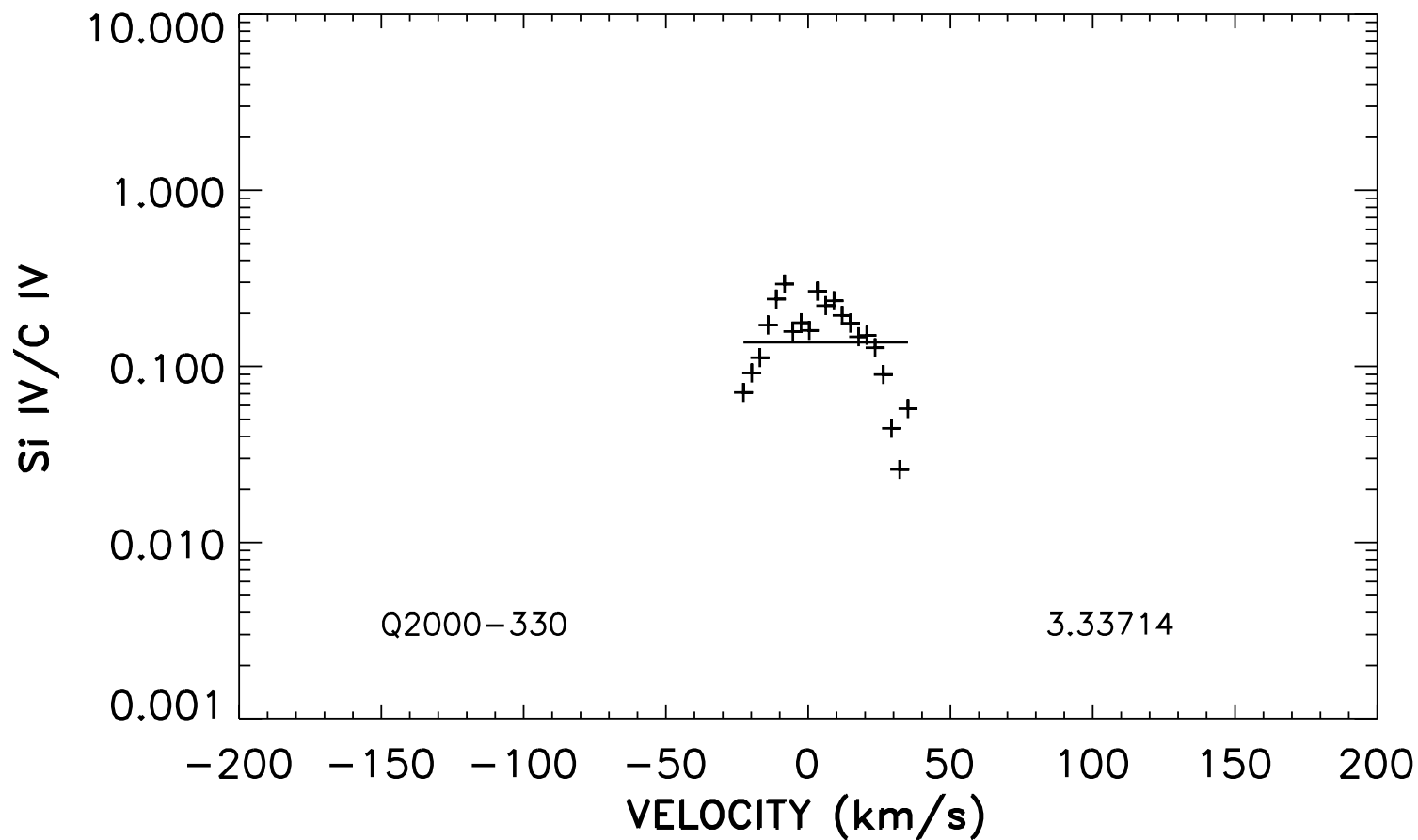


Fig. 13.— Si IV/C IV values across the $z = 3.33714$ complex in Q2000-330, computed from the Si IV and C IV optical depths of Figure 12 with $\tau(\text{C IV}) > 0.05$, as $N(\text{ion}) = \tau\lambda f$, where λ is the wavelength and f the oscillator strength of the transition. The solid line is the average value of Si IV/C IV in the complex, computed from the total column densities of Si IV and C IV measured from Voigt profile fitting.

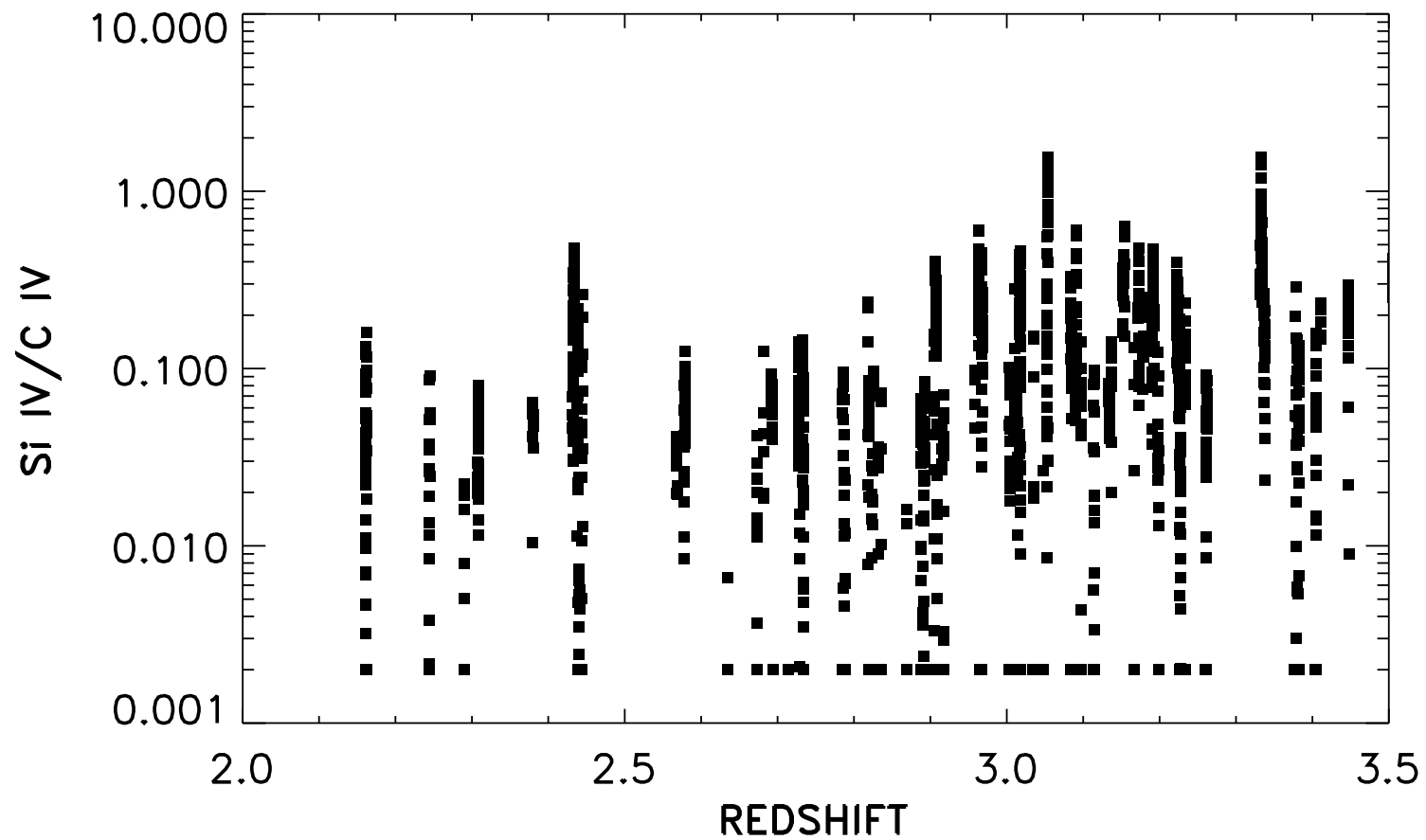


Fig. 14.— The Si IV/C IV density ratios computed from optical depths as in Figure 13 for all the absorption line complexes of Table 2, as a function of the redshift of the complex.

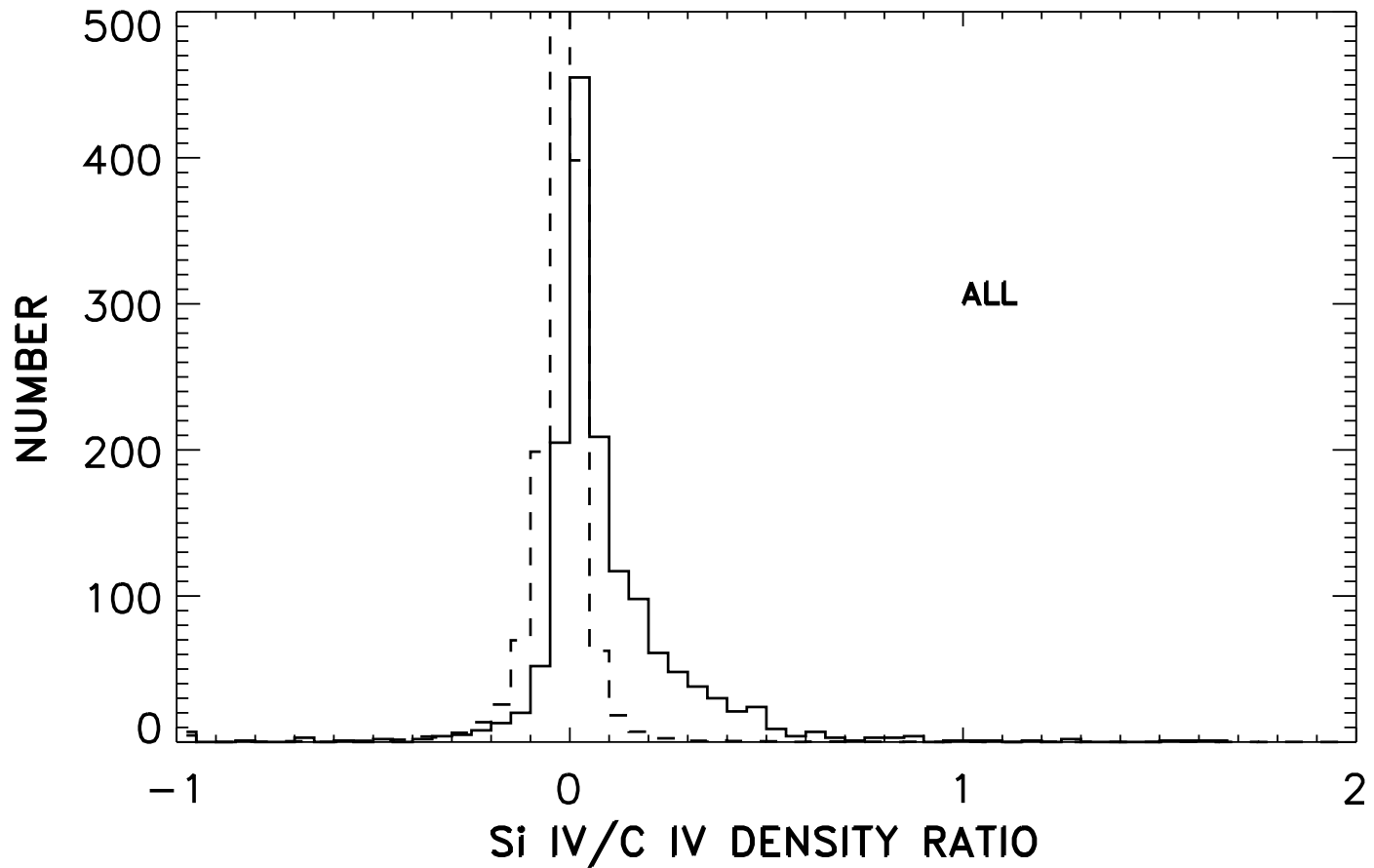


Fig. 15a-c.— The distribution of Si IV/C IV density ratios for all the data of Figure 14 (solid line) compared to the average of random realizations (dashed line). Median and mean values and 1σ errors are given in Tables 3 and 4, respectively.

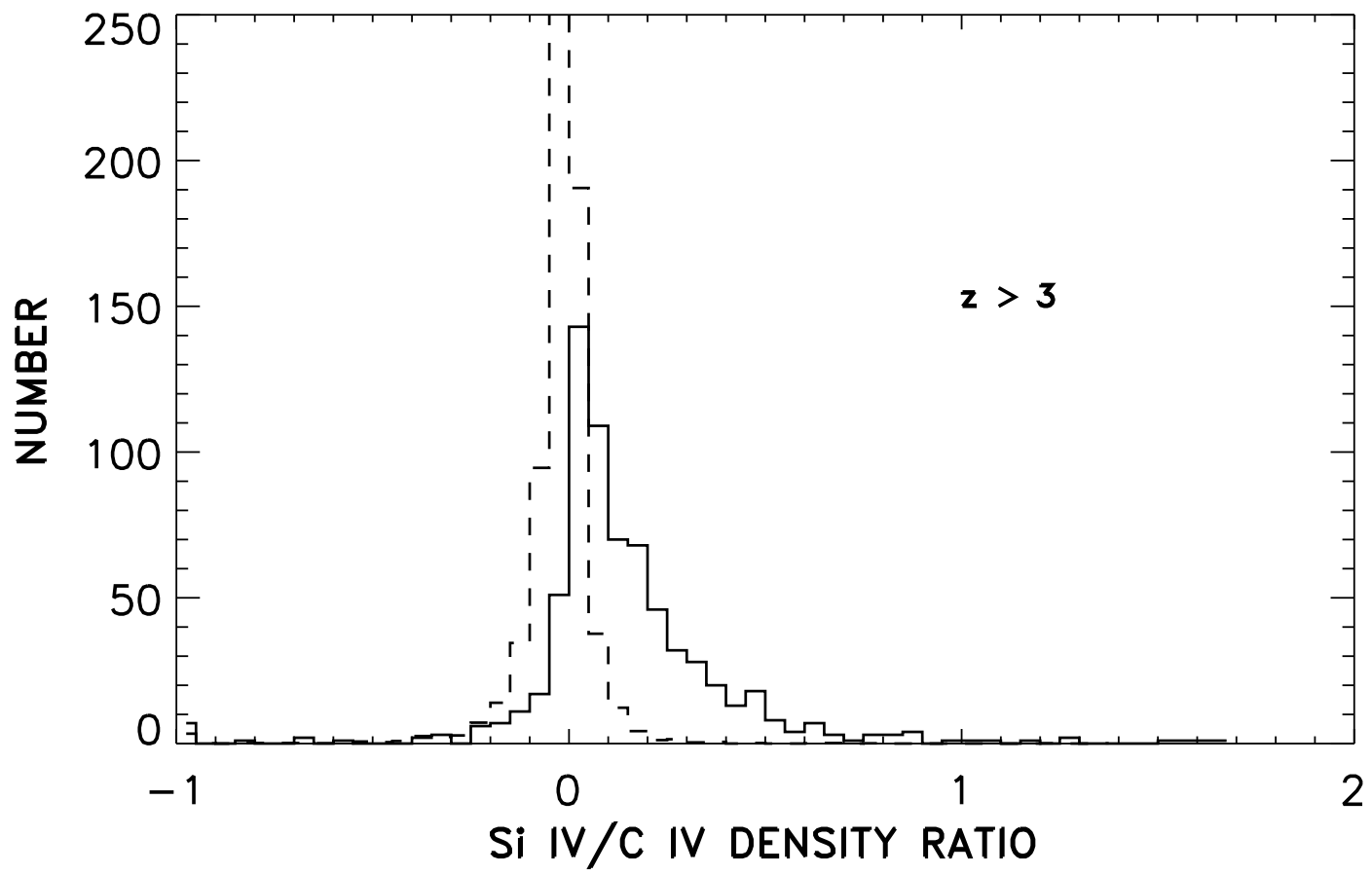


Fig. 15b.— As in (a) for $z > 3$.

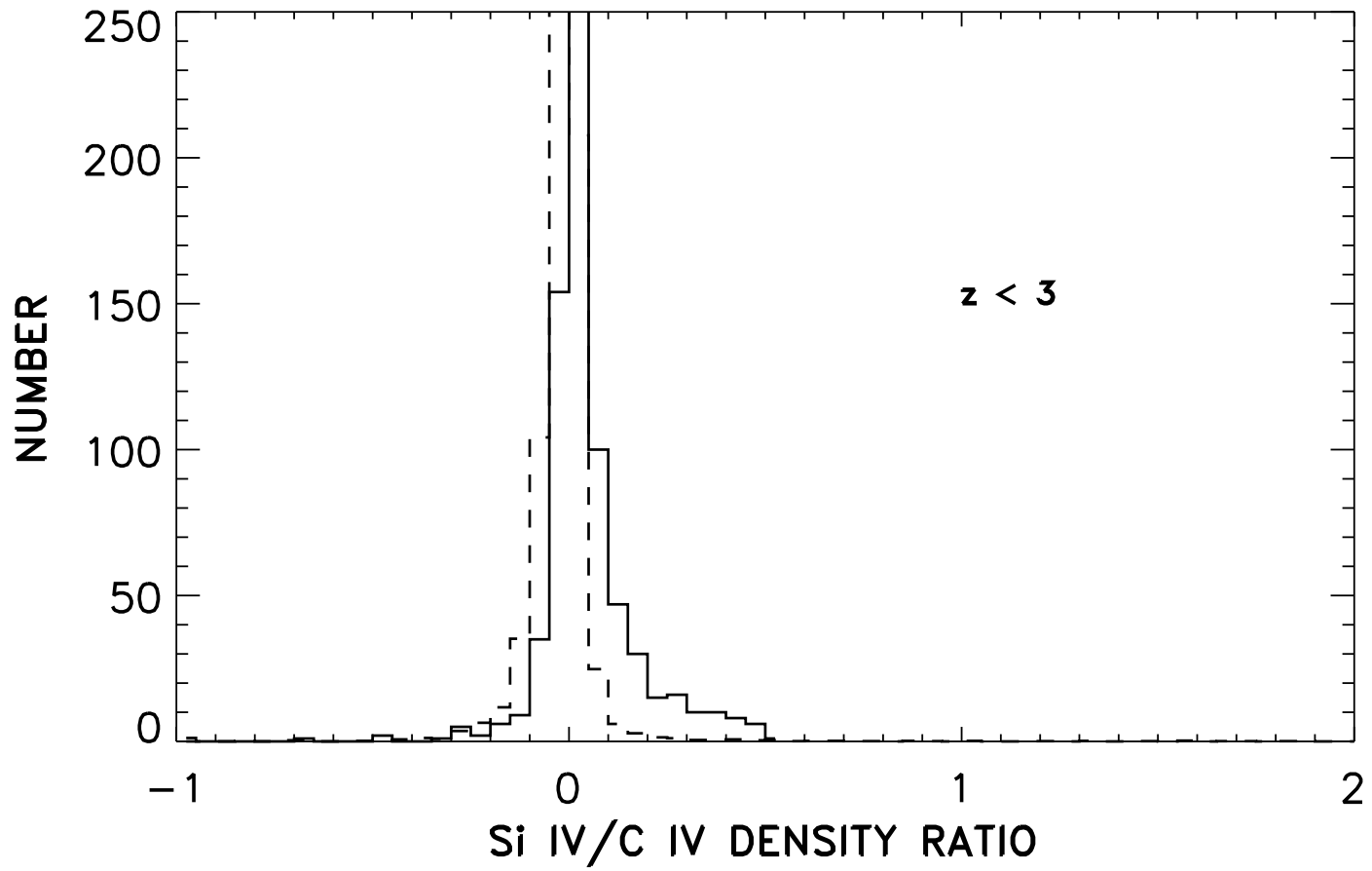


Fig. 15c.— As in (a) for $z < 3$.

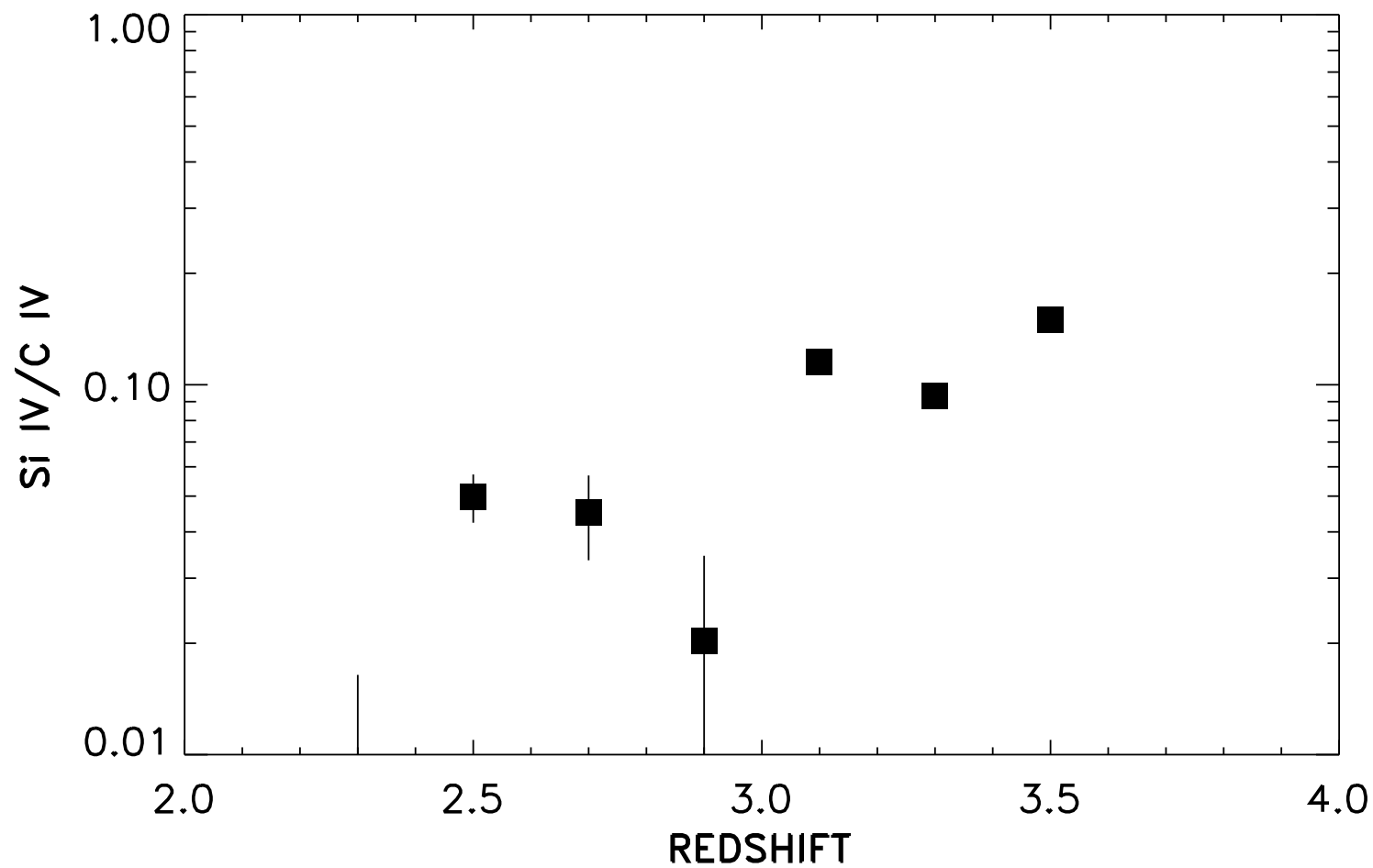


Fig. 16.— Median Si IV/C IV as a function of redshift for the data of Figure 14, with $\pm 1 \sigma$ errors. The median is 0.035 ± 0.005 for $z < 3$ and 0.10 ± 0.01 for $z > 3$.

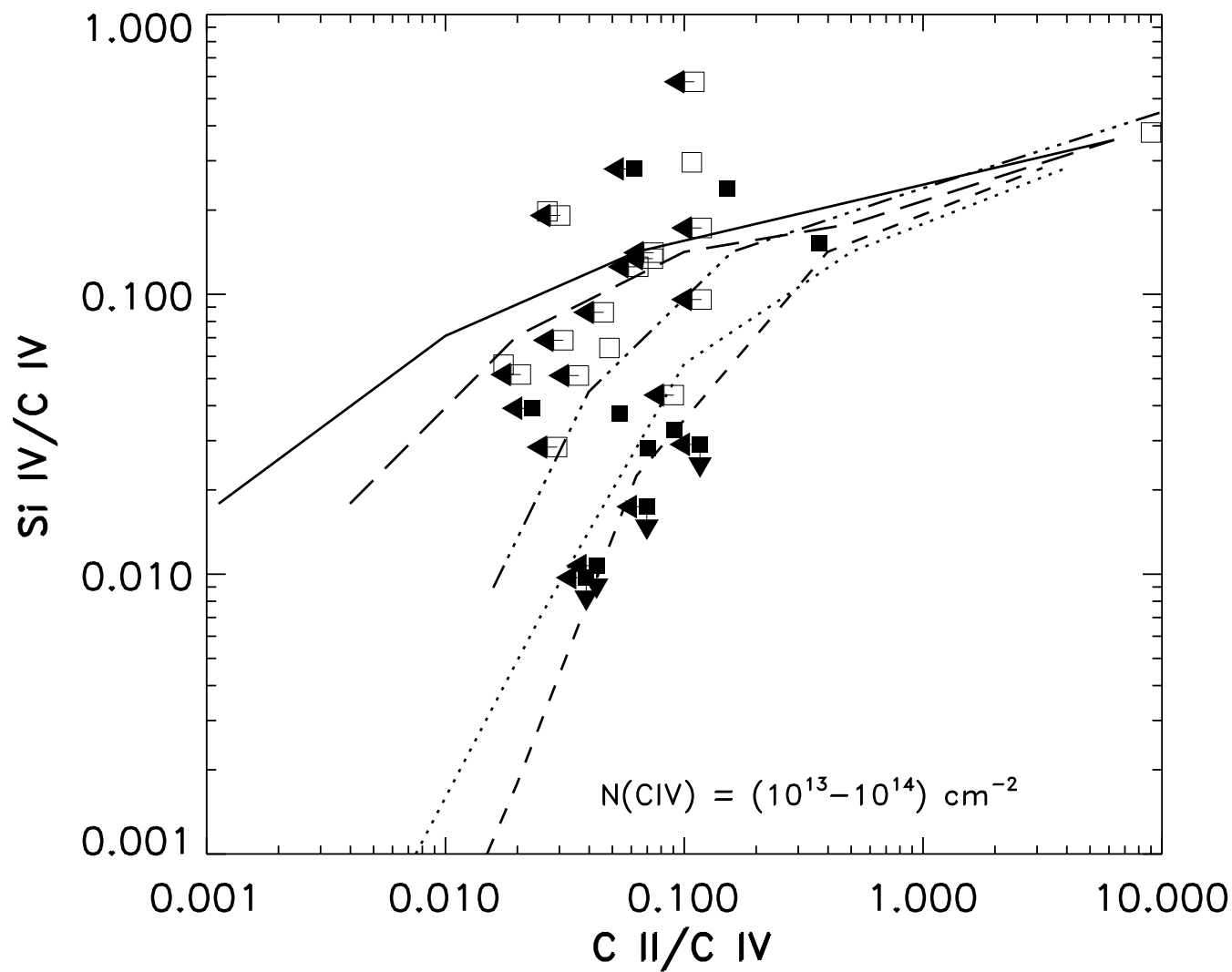


Fig. 17.— Si IV/C IV versus C II/C IV for complexes with $10^{13} \text{ cm}^{-2} < N(\text{C IV}) < 10^{14} \text{ cm}^{-2}$ and with C II longward of the forest for systems with $z < 3$ (filled squares) and $z > 3$ (open squares). Arrows mark systems in which Si IV or C II is not detected, with the square positioned at the 1σ level. The curves are models computed with the CLOUDY code (Ferland 1993) with $\log_{10}(\text{Si}/\text{C}) = -0.66$ for a -1.5 power law ionizing spectrum (dashed line) and with the addition of a break at the He^+ edge at 4 Ryd of a factor of 2 (dotted line), 10 (dash-dot line), 100 (long dash line) and 1000 (solid line).

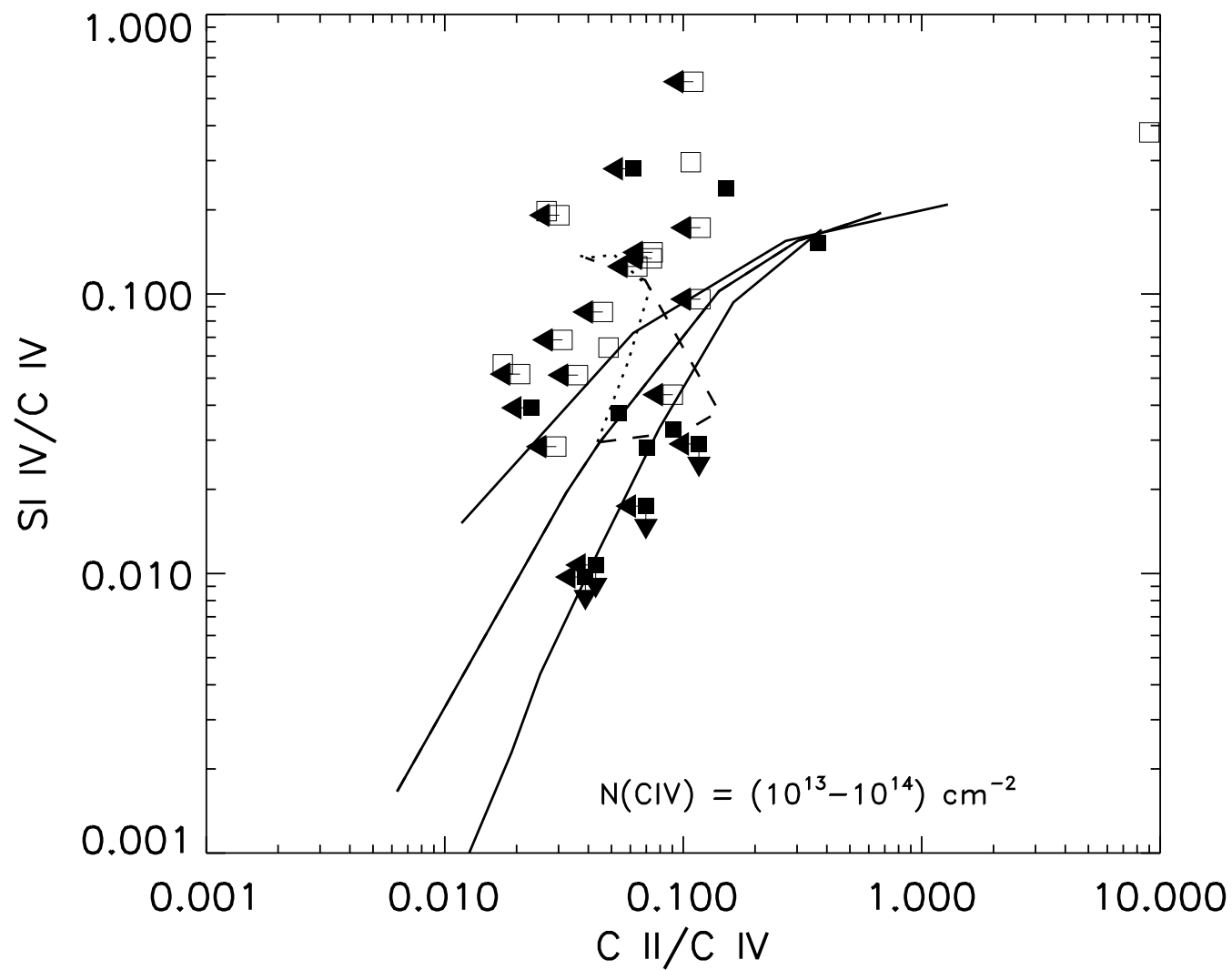


Fig. 18.— Si IV/C IV versus C II/C IV for the data of Figure 17 (filled and open squares). The solid lines are CLOUDY models with power law spectra with index -1.5 (bottom), -2.0 (middle), and -2.5 (top), computed with $\log_{10}(\text{Si}/\text{C}) = -0.66$. The dashed and dotted curves show the effect of the introduction of a break in the spectrum at the He^+ edge. See text (§4.2) for details.

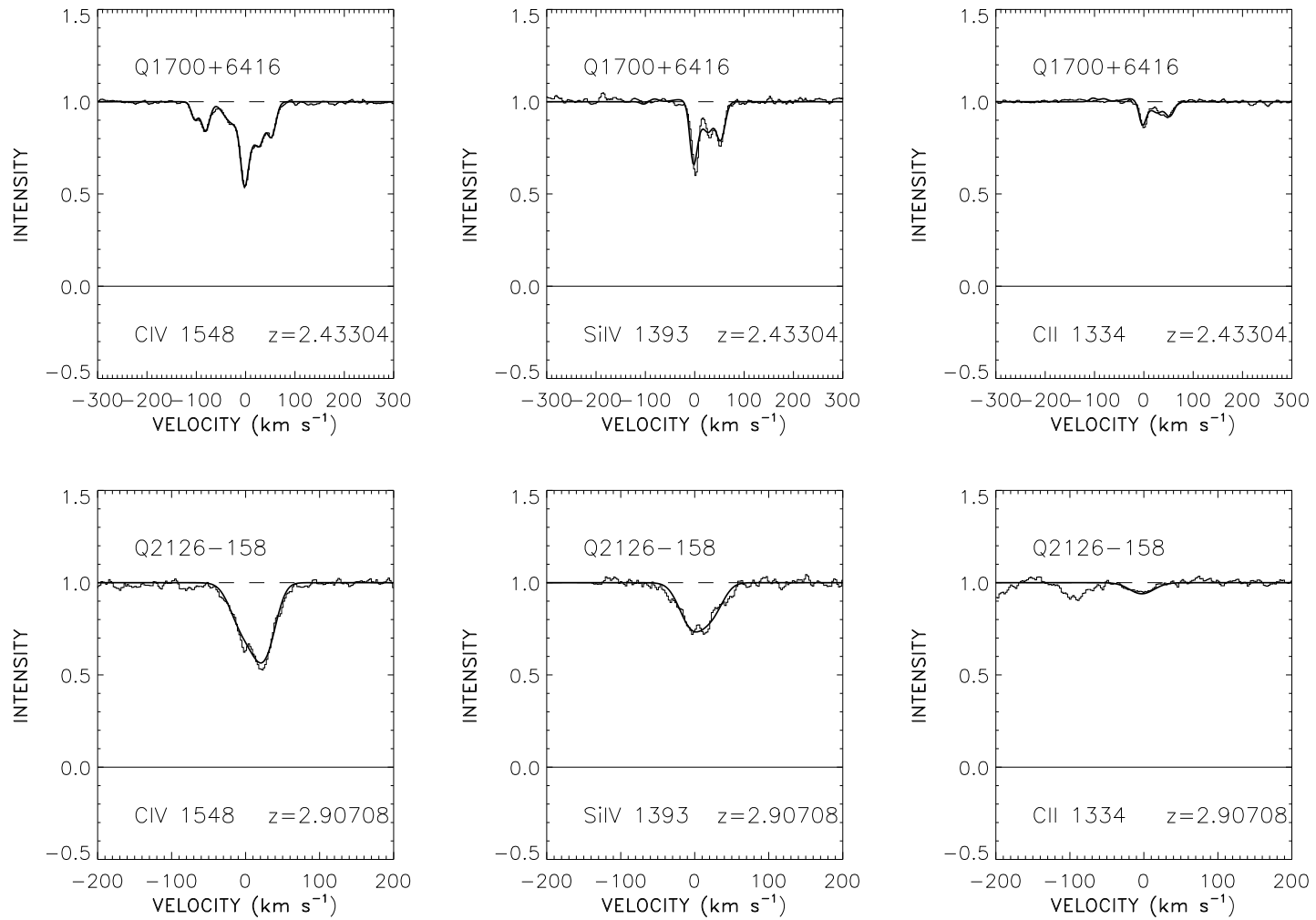


Fig. 19a.— Sample C IV, Si IV and C II profiles for systems with a high value of Si IV/C IV at $z < 3$.

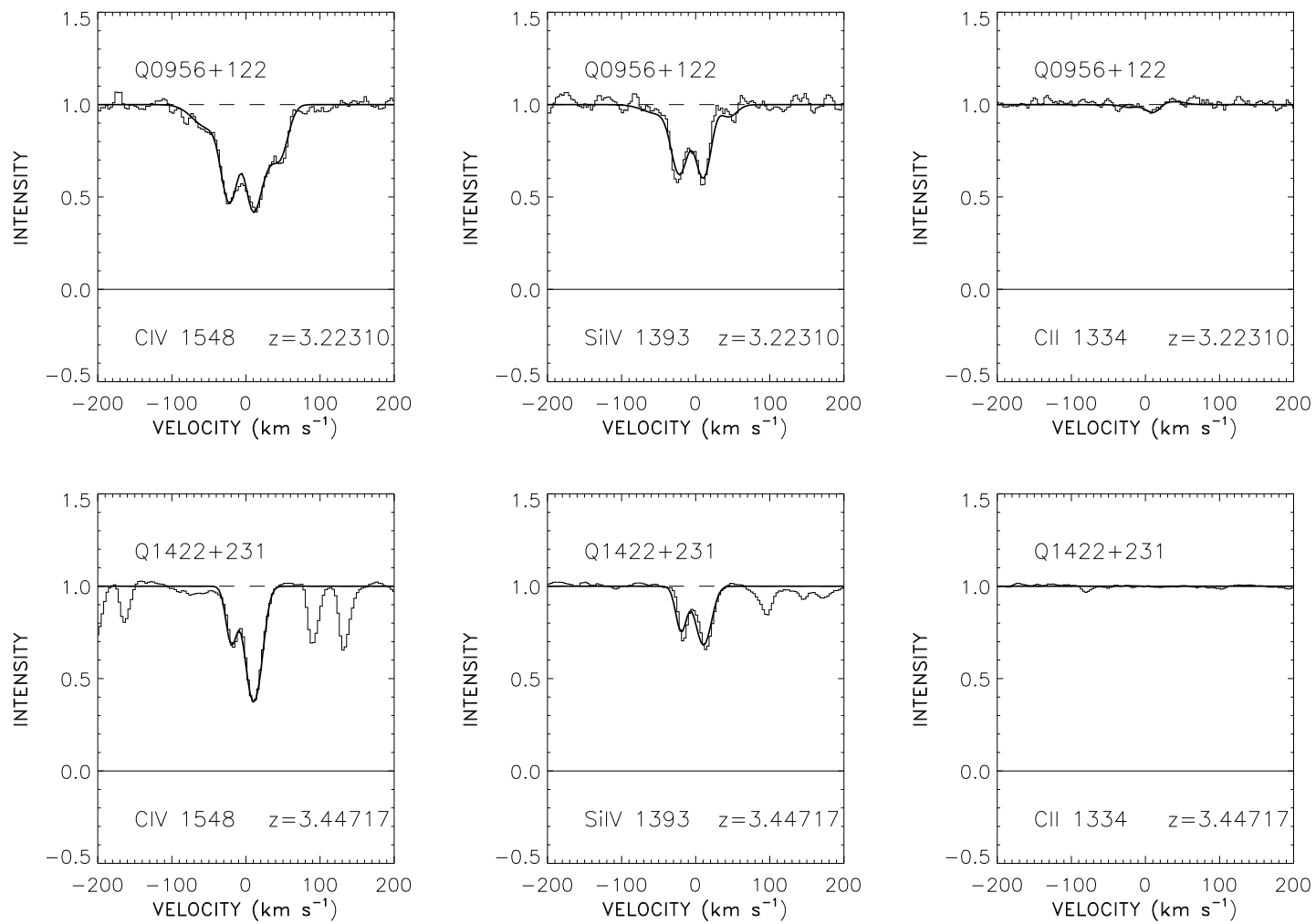


Fig. 19b.— As in (a) for systems with $z > 3$, illustrating the absence of C II in these high redshift systems.

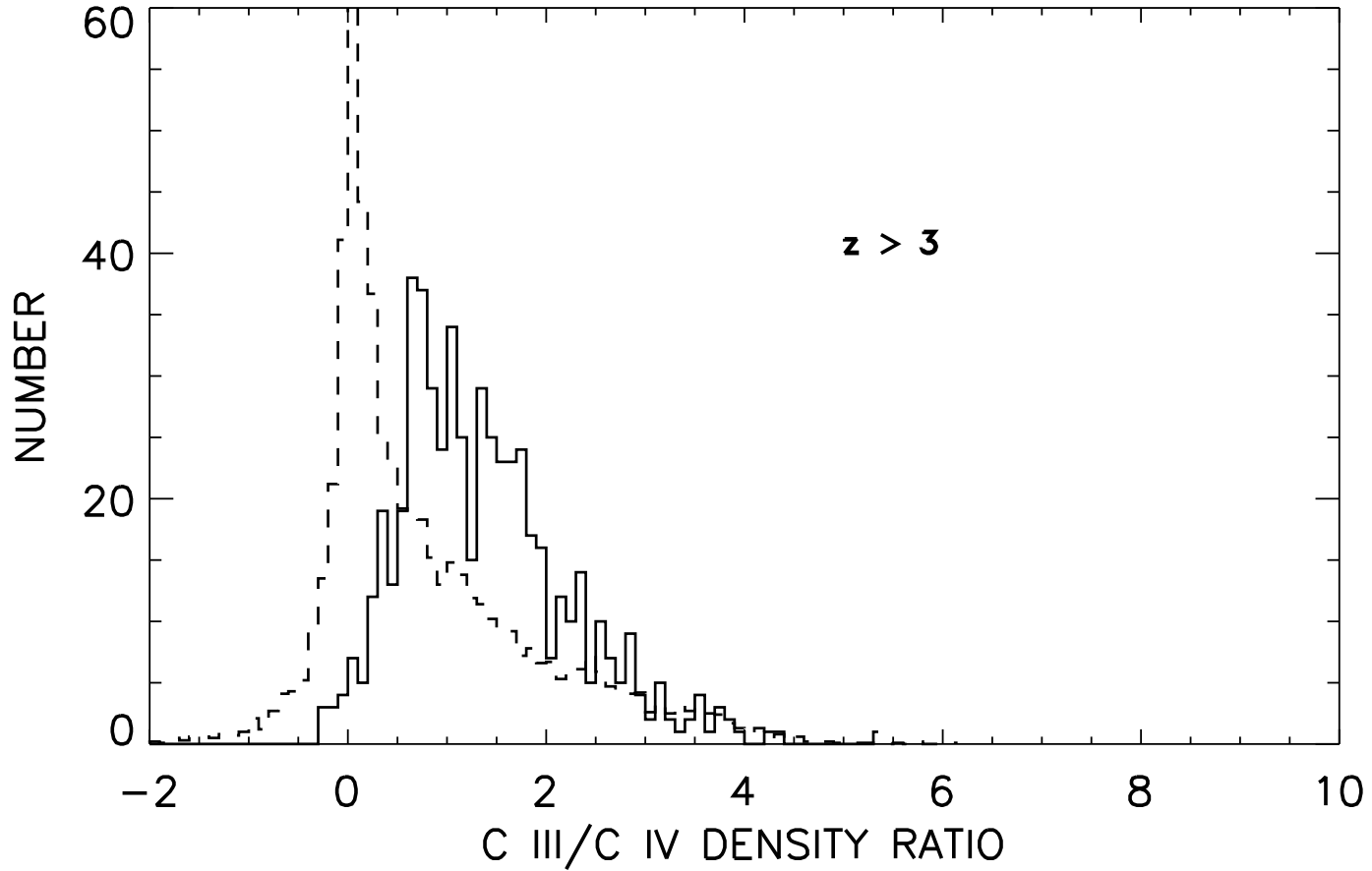


Fig. 20a–g.— (Solid lines): distributions of C III/C IV, N V/C IV, and O VI/C IV computed from the optical depth ratios for $\tau(\text{C IV}) > 0.05$, as in Figure 15, compared with average blank realizations (dashed lines). Where possible, distributions are also shown separately for $z > 3$ and $z < 3$. Median and mean values and 1σ errors are given in Tables 3 and 4, respectively.

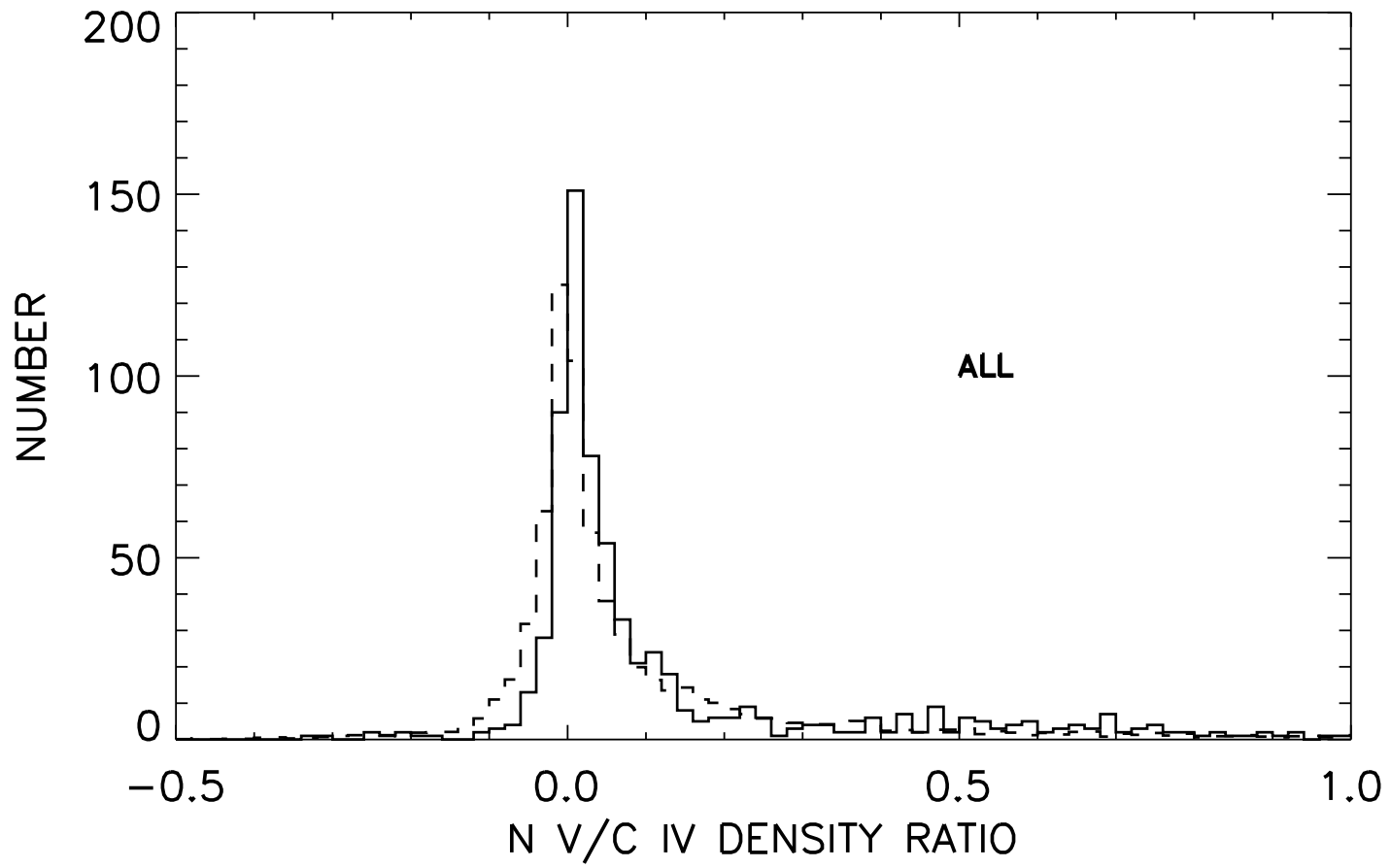


Fig. 20b.—

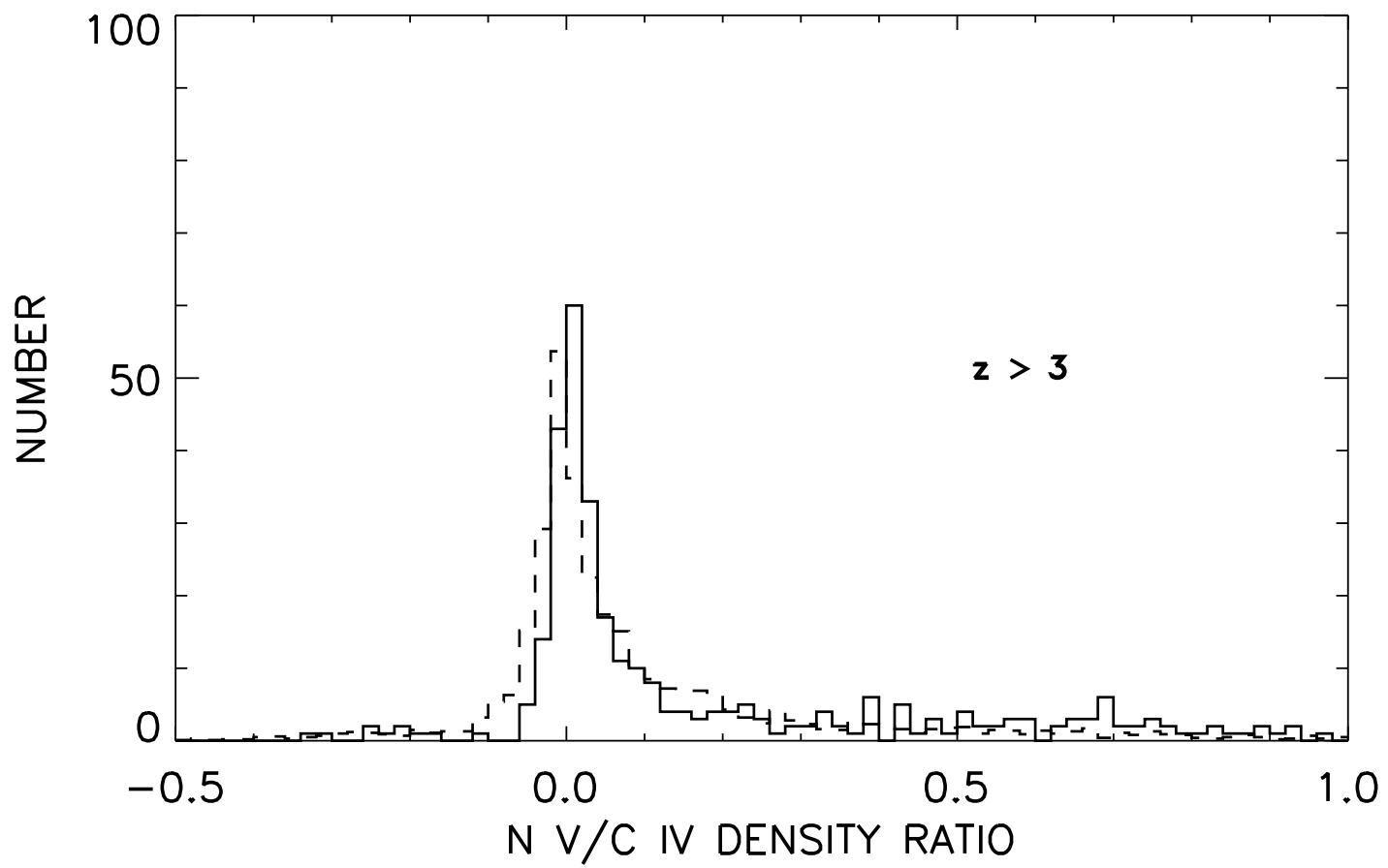


Fig. 20c.—

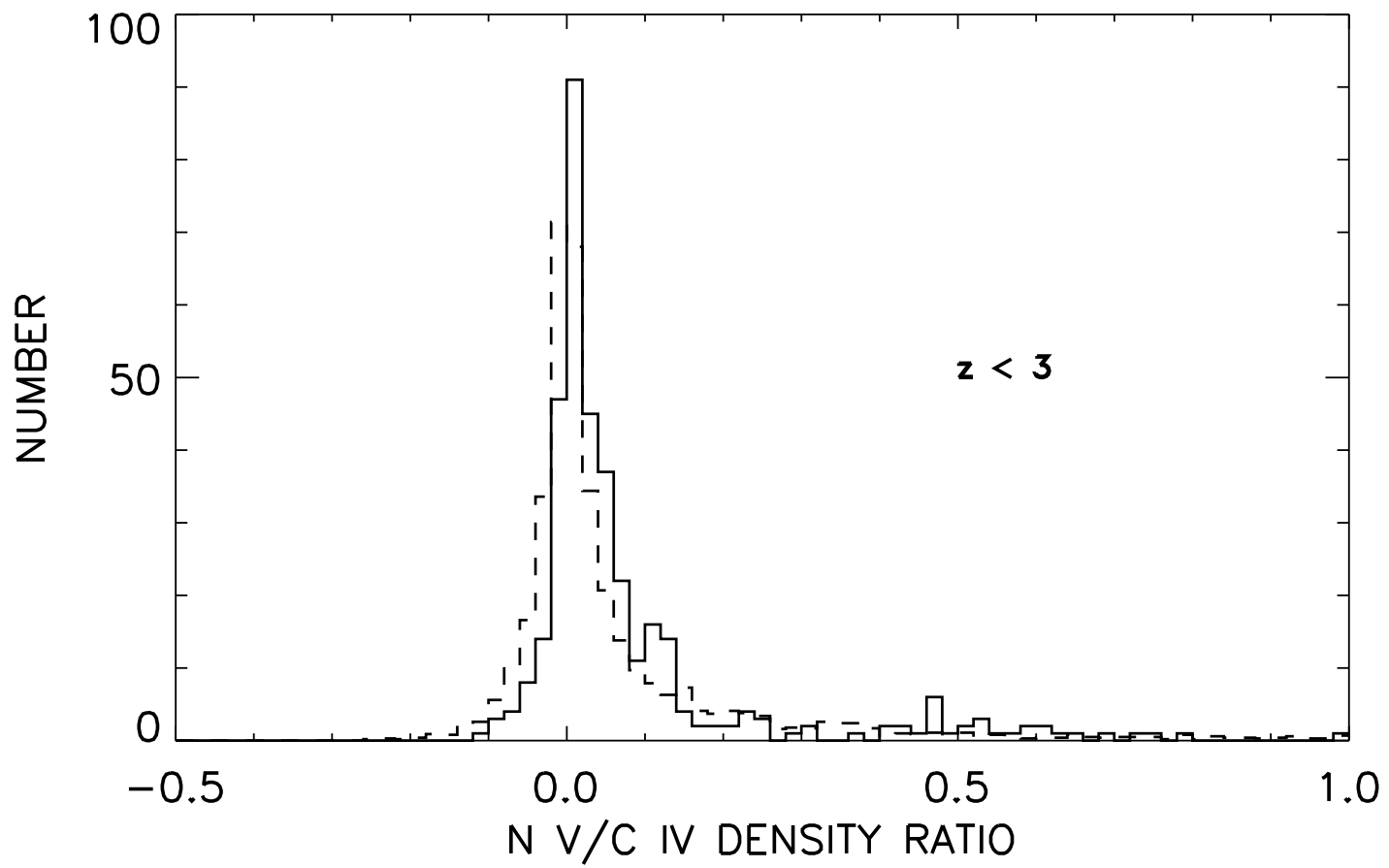


Fig. 20d.—

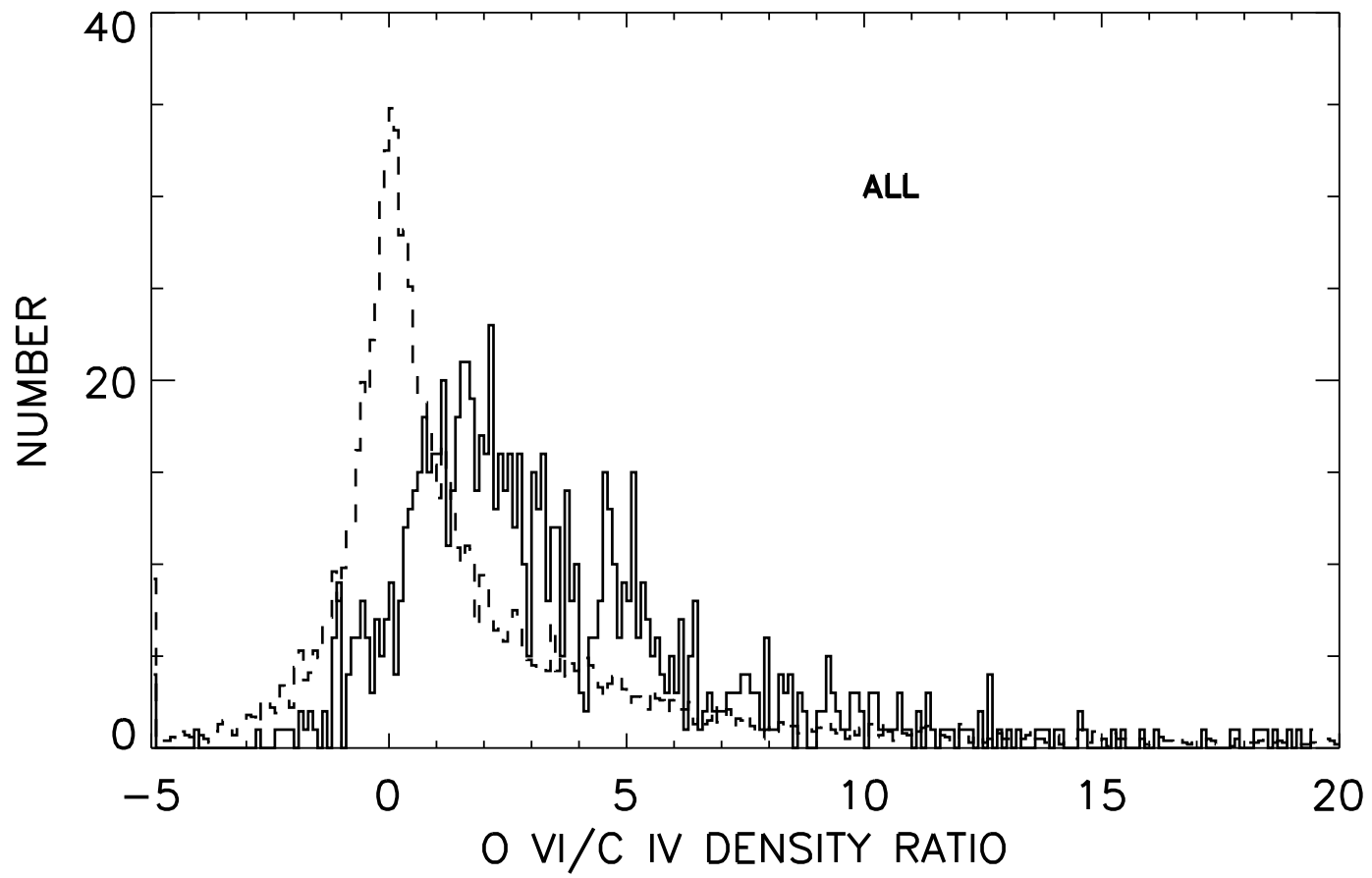


Fig. 20e.—

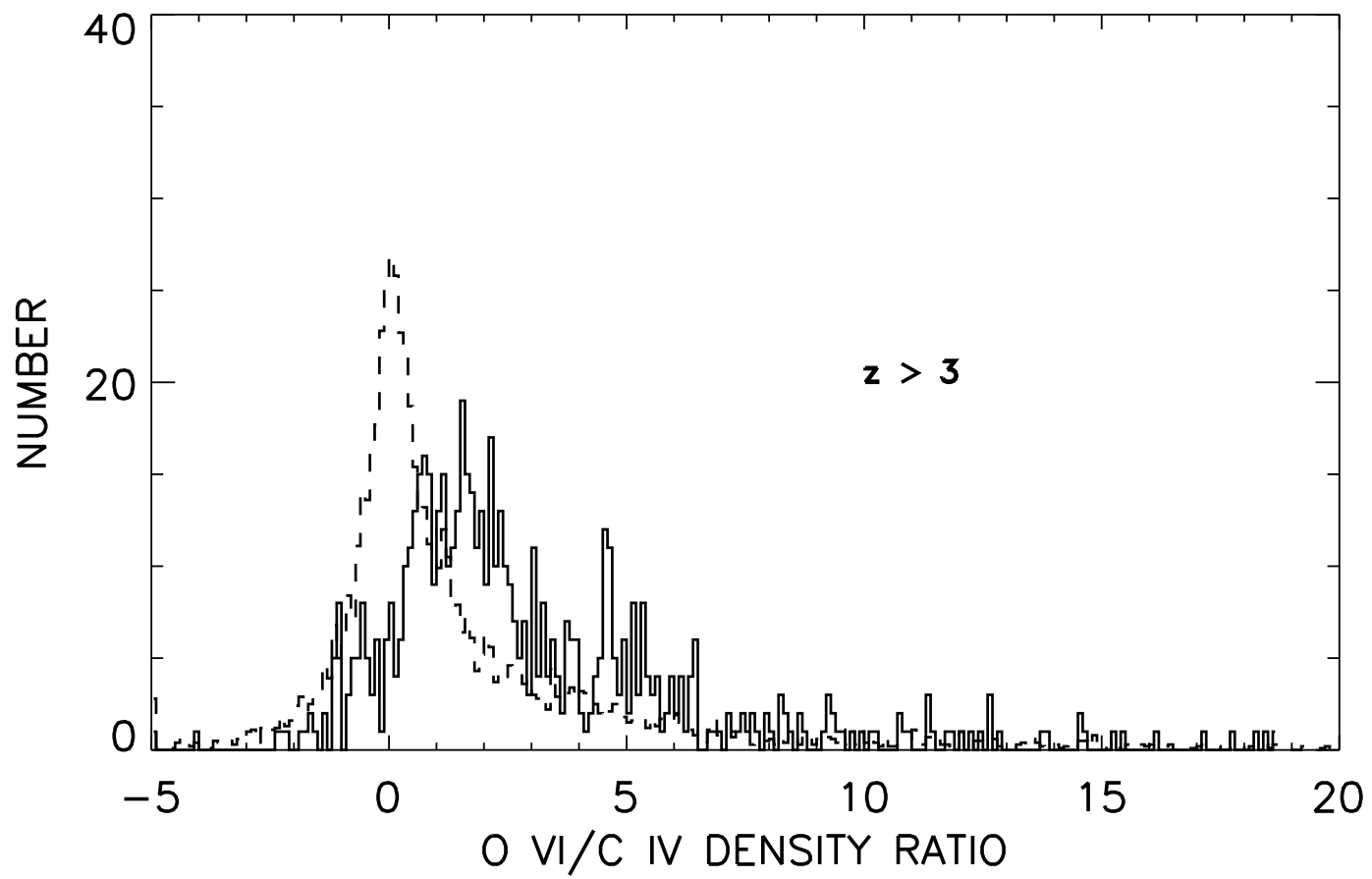


Fig. 20f.—

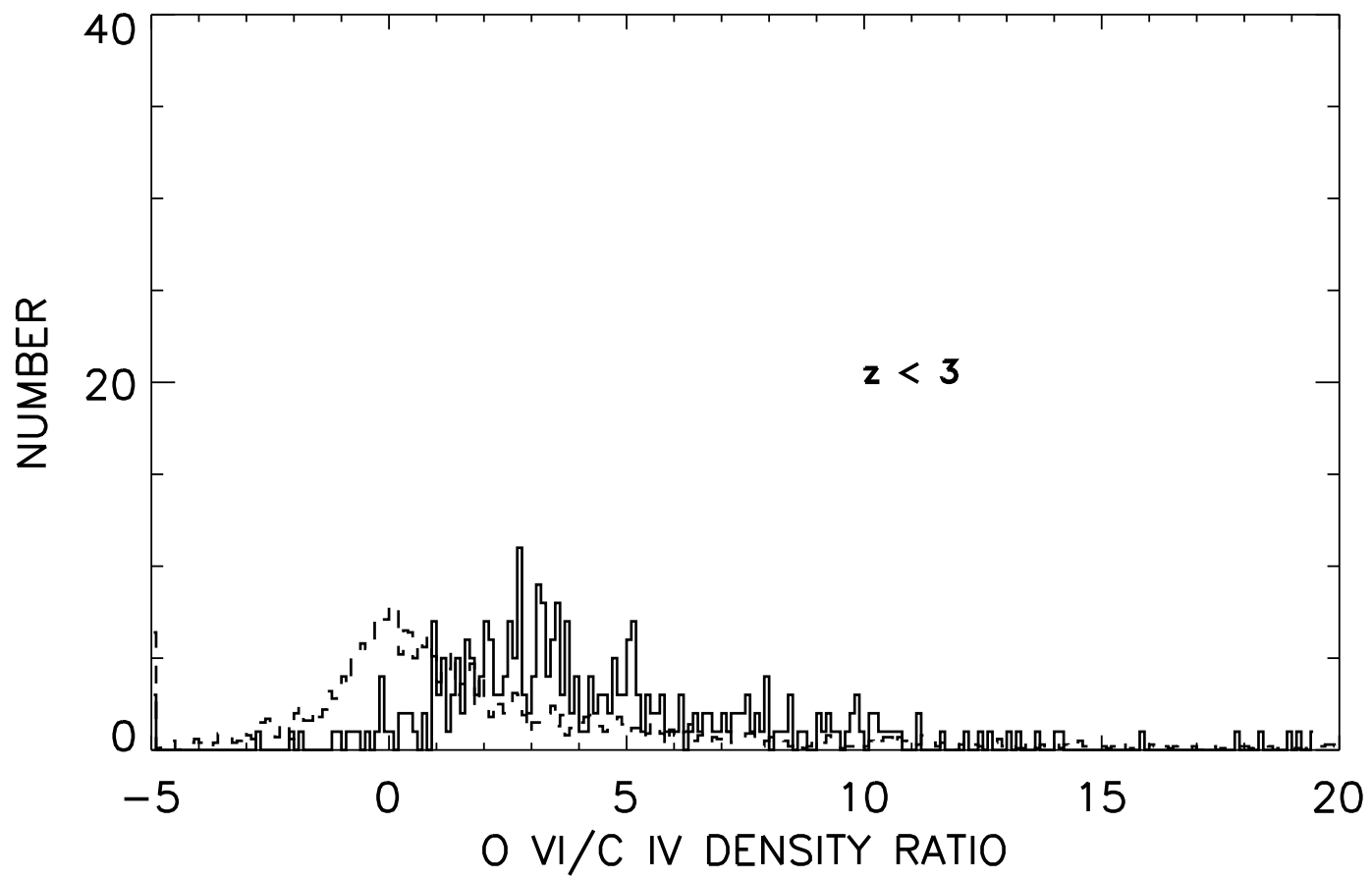


Fig. 20g.—

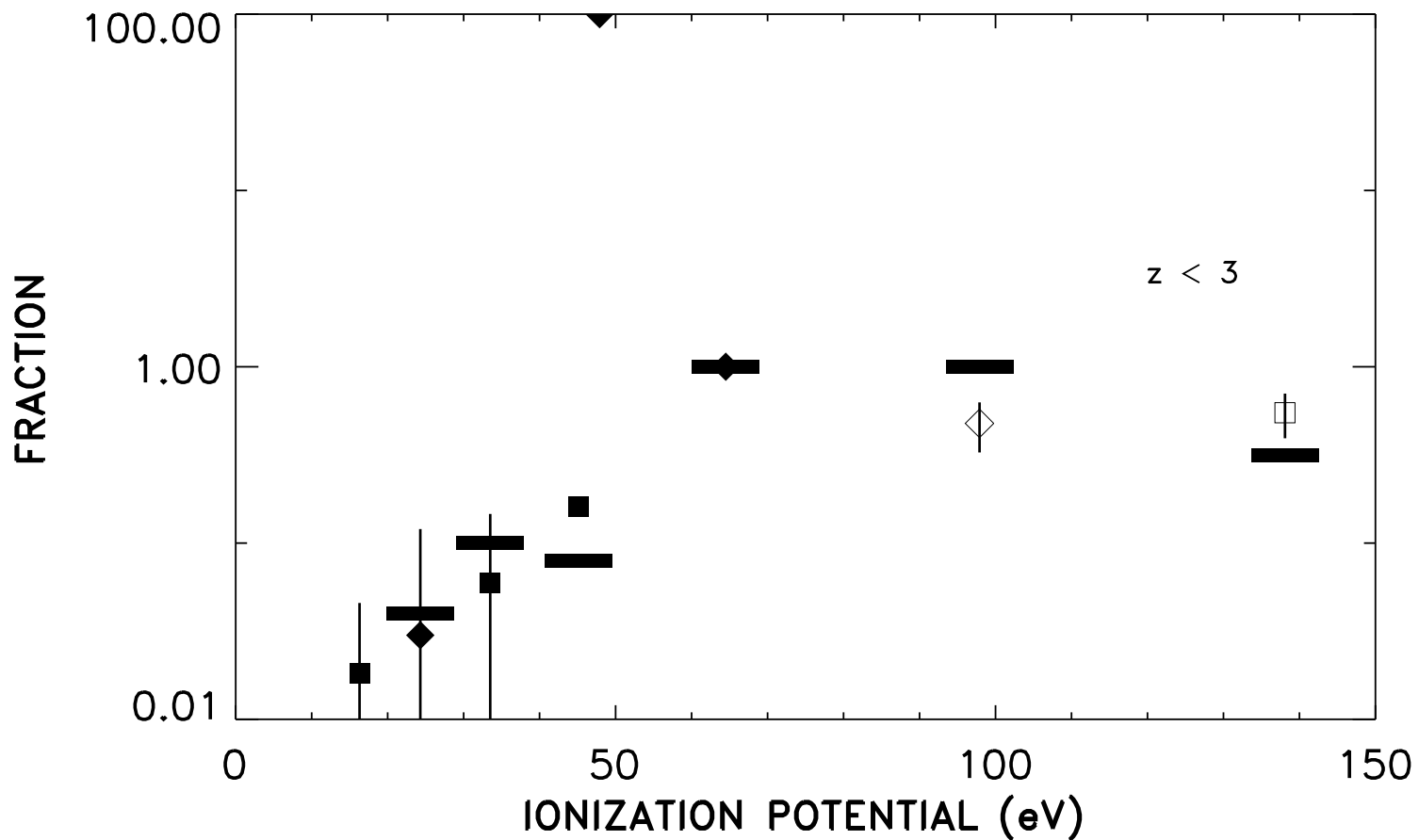


Fig. 21a.— The quantity $A_C N(X)/A_X N(\text{C IV})$ for $z < 3$ for the ions, X , of Table 3, where (A_X/A_C) is the abundance of the element X with respect to C, as a function of the ionization potential of the ion, in eV. Errors are $\pm 1 \sigma$. The solid bars show a model in which the ionizing spectrum is a -1.8 power law with $\Gamma = -1.6$.

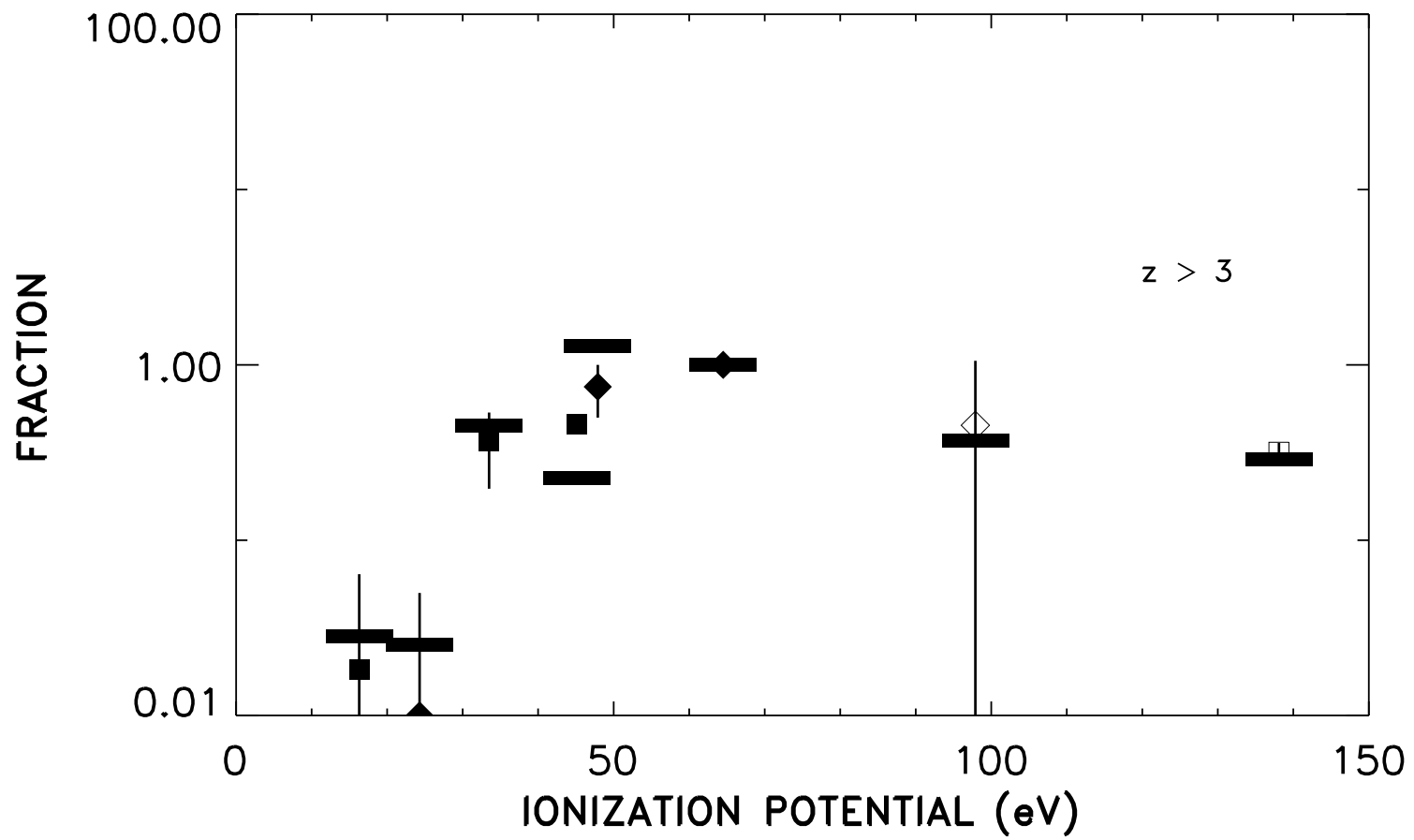


Fig. 21b.— As in (a) for $z > 3$. See text (§4.3) for a description of the comparison model (solid bars).